Mechanics of Thin-Skinned Thrust-and-Fold Belts: Insights from Numerical Models

Glen S. Stockmal[1], Chris Beaumont[2], Mai Nguyen[2], and Bonny Lee[2]

[1]Natural Resources Canada, Geological Survey of Canada (Calgary), 3303-33rd Street NW, Calgary, AB, T2L 2A7; [2]Dalhousie Geodynamics Group, Department of Oceanography, Dalhousie University, Halifax, NS, B3H 4J1

Abstract

We examine aspects of the mechanics of thin-skinned thrust-and-fold belts (TFBs) using an arbitrary Lagrangian-Eulerian finite element approach. Dynamical numerical modelling techniques are powerful tools for understanding the mechanics of TFBs, especially at scales smaller than that of the entire belt. A series of models of increasing complexity illustrate the effects of flexural isostatic subsidence, strain-softening, multiple layers of strong and very weak materials, erosion, and sedimentation. Narrow zones of high shear strain emulate fault zones, and yield structures very similar in style to those in TFBs. These structures include far-travelled thrust sheets, irregular-roof and smooth-roof duplexes, back-thrusts, pop-ups, detachment folds, fault-bend folds, break-thrusts, and piggyback basins. They can develop as in-sequence or out-of-sequence structures, remain active for extended periods, or be later reactivated. Although the overall external geometries of these models conform to critical wedge theory, there are significant departures at sub-whole-

wedge scales. These departures reflect: (1) the dynamical nature of the models, which are built upon variational (minimum dissipation) principles, (2) that the wedge is constructed from finite-thickness layers that deform to create particular geometries during their initial deformation, for example triangular plugs or pop-up structures, and that subsequently determine the primary ‘building block scale’ of the wedge (3) spatial and temporal variations in internal and basal strength, and (4) the fact that segments of the TFB may not be at yield due to the wedge and surface processes behaving as a coupled system. The structural styles produced in models involving feedback with surface processes (erosion and sedimentation) are very similar to those mapped in the Foothills of the Southern Canadian Rockies and elsewhere. Although syndeformational sediments have been removed by erosion across the Foothills belt, the structural characteristics of the interaction between deformational style and surface processes remain.

Introduction

The mechanics of thin-skinned thrust-and-fold belts are well described at whole-wedge scales by critical wedge models (e.g., Chapple, 1978; Davis et al., 1983; Dahlen, 1984). These are closed-form solutions where the static equilibrium equations are solved assuming material within the wedge is everywhere on the verge of failure. Such solutions are examples of 'existence theory' in which the theory predicts the geometry of critical wedges and shows for what range of control parameter values they exist. However, these theories do not show how wedges deform internally to achieve the critical geometry, or how they grow during subsequent accretion. Although these and associated critical wedge formulations (e.g., Dahlen et al., 1984; Dahlen and Suppe, 1988; Dahlen, 1988, 1990; among others) provide insight into the large-scale mechanics of thrust-and-fold belts, the lack of dynamics, the requirement of simultaneous yield, and restrictions on material variability within the wedge strongly limit their usefulness for understanding the development of structures at scales smaller than the entire wedge.

Here we describe dynamical numerical models of thin-skinned wedges using a plane-strain, finite element (FE), continuum mechanics approach (see Fullsack, 1995, and Beaumont et al., 2004). These models calculate wedge growth, allow examination of the influence of a range of parameters on structural style, and offer the prospect of a deeper understanding of the feedback relationships that may shape structures within thrust-and-fold belts. In particular, the importance of surface processes (erosion and sedimentation), known to influence the large-scale or whole-wedge evolution of critical

wedges (e.g., Beaumont et al., 1992; Willett, 1999; Whipple and Meade, 2004), can be assessed at scales smaller than the entire wedge.

Our principal goals are to establish the utility of the FE approach in addressing thin-skinned thrust-and-fold belt mechanics, and to demonstrate the importance of feedback between structural evolution and surface processes, especially syndeformational sedimentation. An associated longer-term goal is to isolate the principal variables that control structural styles in the external, brittle portions of thrust-and-fold belts, and to place bounds on their values. Our approach is to design a series of numerical model experiments, where model parameters are systematically varied to investigate their influence on structural style. As commonly assumed in modelling experiments, geometrical similarity of model structural styles to those observed in nature is a necessary (though not sufficient) condition that the models provide useful constraints on the mechanics and dynamics of natural structures (e.g., Hubbert, 1951).

Insights and Constraints from Natural Examples

As emphasized and listed explicitly by Chapple (1978), there are four fundamental characteristics of “folded mountain belts”:

1. The belts are thin-skinned, where the basal decollement often, but not always, lies at or just above the crystalline basement.
2. The basal layer, which commonly hosts the basal decollement, is generally composed of relatively weak rock.
3. The thrust-and-fold belt after deformation, as well as the sedimentary prism before deformation, is wedge-shaped, thinning toward the foreland.

4. The entire wedge has been shortened and thickened, such that shortening within the wedge accommodates motion of the hinterland end.

These characteristics are typical of numerous thrust-and-fold belts. Here we make particular reference to the Southern Canadian Rocky Mountains (SCRM) as an archetypal thin-skinned belt (Figure 1).

The surface of the Archean to Early Proterozoic crystalline basement underlying the SCRM exhibits little to no relief at the scale of the belt, and dips gently toward the orogen reflecting the regional isostatic response of the lithosphere to supracrustal loading by thrust sheets (Price, 1973, 1981; Beaumont, 1981; Price and Fermor, 1985). The basement is overlain by a Paleozoic to middle Mesozoic platform to shelf margin succession of carbonates and subordinate siliciclastic rocks that tapers in stratigraphic thickness from approximately 2 km at the deformation front to approximately 3 km at the western edge of the Front Ranges (Figure 1), approximately 175 km distant in palinspastic restoration (Price and Fermor, 1985). This dominantly carbonate succession is overlain in turn by middle Mesozoic to early Cenozoic foreland basin siliciclastics. At the deformation front, the preserved thickness of the foreland succession is approximately 3 km (Figure 1), with perhaps an additional 2 to 3 km removed by post-deformational erosion (Hacquebard, 1977; Nurkowski, 1984.).

These strata include natural variations in mechanical strength, which resulted in concentration of strain along weak layers, forming major and minor décollements. In the SCRM, there are two principal detachment horizons (Figure 1): (1) at the crystalline basement / sedimentary cover contact, where Early Cambrian clastic rocks (Gog Group) are inferred to overlie crystalline rocks, and (2) within the Upper Jurassic Fernie

Formation, a package of dominantly marine shales that includes the basal units of the flexural foreland basin. In addition, there are a number of secondary detachment zones. In the Foothills (Figure 1), where structures within the dominantly Mesozoic foreland basin strata are exposed, these are commonly associated with marine shale units. In this paper, we use the terms “detachment” or “detachment zone” to describe the material layer within which layer-parallel décollements might propagate, and reserve the term “décollement” for zones of accumulated high shear strain.

Model Design

Configuration and Boundary Conditions

The minimum requirements for any realistic model of thin-skinned deformation are one or more material layers above a weaker basal layer (or surface), which in turn overlies a non-involved “basement” (characteristics 1 and 2, above). This minimum configuration was accommodated by Chapple (1978), Davis et al. (1983), and Stockmal (1983), where in all cases the weak base has zero thickness. In our continuum mechanical FE models the weak basal layer has a finite thickness.

Our prototype models are designed to represent layered sedimentary successions, and have no initial lateral variation in layer thickness. Although this does not satisfy part of characteristic 3, adoption of the simplest geometry will allow us to later examine the influence of initially tapered layers. As the models evolve in time, they develop overall tapered shapes through internal thickening and shortening, satisfying the other part of characteristic 3, as well as characteristic 4. In those models

incorporating syndeformational sedimentation, characteristic 3 develops naturally as the system evolves above a regionally isostatically compensated (flexural) plate.

All models are two-dimensional (vertical cross section, plane strain). The initially uniform-thickness layer(s) lie on a surface that can have an arbitrary shape (here it is initially horizontal), and be either rigid or respond as an elastic plate (uniform or spatially variable flexural rigidity) representing regional flexural isostasy. This underlying surface, to which the weak basal layer is attached, is moved parallel to the flexed base at a constant rate (Table 1) toward a vertical backstop at the left-hand side of the model (Figure 2). Material enters the model from the right-hand side at this same velocity. The vertical backstop does not support shear stresses. Near the base of the vertical backstop, a thin slot equal in height to the initial thickness of the weak basal layer allows material to exit the models, avoiding the accumulation of weak basal material in the corner. In practice, this slot has very little effect on the overall style of model evolution.

The initial configurations for basic models with one, two, or three detachment horizons are shown in Figure 2. The one-detachment model corresponds to the simplest case of a relatively strong layer overlying a weaker base, as modelled by the closed-form existence theories noted above. The strong layers in the two- and three-detachment models are of equal initial thickness (Table 2). The weak detachment horizons, whether on the base or internal, are of equal absolute initial thickness in all models (Table 2). Each model is initially 5 km in total thickness, similar in magnitude to the SCRM archetypal belt.

Note that layering within the two- and three-detachment models does not initially extend all the way to the backstop (Figure 2). This is intended to minimize the effects of

the backstop boundary conditions by creating a first phase of uniform wedge growth without internal layering that acts as a buffer. This uniform wedge also serves to emphasize the influence of the internal detachment horizons, where a marked change in structural style is observed in all the models at the point where these horizons become involved in the deformation.

Although the thermal evolution of the models could be included (e.g., Beaumont et al., 2004), we have chosen to restrict the rheology to plastic materials with no temperature dependence in order to keep the models as simple as possible. We recognize that parts of the wedges, particularly the deeper regions, may become ductile in equivalent natural systems.

Model Materials

In the brittle regime, most rocks behave as Mohr-Coulomb (frictional) materials, with failure strengths that increase with confining pressure (e.g., Paterson, 1978). These materials, with a finite failure or yield strength, have a plastic rheology. A Mohr-Coulomb plastic material is parameterized by a cohesion value and an angle of internal friction. Here we adopt a rigid-plastic pressure-dependent formulation (elastic strain is not incorporated) known as a Drucker-Prager material (equivalent to a Mohr-Coulomb failure criterion in plane-strain), with an incompressible (zero volume change during deformation) non-associative flow law. Yielding occurs when

(1) $$\sqrt{J_2'} = C_0 \cos\varphi_{eff} + P \sin\varphi_{eff}$$

where $\sqrt{J_2'} = (\tfrac{1}{2}\sigma_{ij}'\sigma_{ij}')^{1/2}$ is the second invariant of the deviatoric stress, C_0 is the cohesion, P is the solid pressure (mean stress), and φ_{eff} is the effective angle of

internal friction. This angle, φ_{eff} , can be either the true internal angle of friction of the material or an apparent value if pore fluid pressure leads to reduced effective stress levels. In both cases φ_{eff} can also vary with strain.

Effect of Pore Fluid Pressure on Material Properties

Transient and permanent fluid pressure variations may be significant factors in weakening brittle rocks (e.g., Hubbert and Rubey, 1959; Paterson, 1978; Rice, 1992; Ridley, 1993; Sibson, 1990; Streit, 1997; Ingebritsen and Manning, 1999; Connolly and Podladchikov, 2000). Pore fluid pressure, P_f , acts to reduce the dynamic pressure (mean stress), and P in equation 1 is replaced by the effective pressure, P - P_f . Clearly, rock strength can become negligible when $P_f \sim P$.

One approach to consider the effect of pore fluid pressure is to introduce an effective internal angle of friction φ_{eff} such that

(2) $$P \sin \varphi_{eff} = \left(P - P_f\right) \sin \varphi = P(1-\lambda) \sin \varphi$$

where $\lambda = P_f / P$ is the pore fluid pressure ratio. (This definition differs from that of Hubbert and Rubey (1959); see Appendix). The approach of using an effective internal angle of friction allows us to investigate the sensitivity of the model results to a range of conditions that can be equated to various pore fluid pressure regimes. Depending on the pore pressure, φ_{eff} may vary from "dry" values (λ=0; e.g., $\varphi_{eff} \sim 35^\circ$), through hydrostatic, to highly overpressured (λ~1; $\varphi_{eff} \sim 0^\circ$). Note that this approach does not imply that the intrinsic internal angle of friction of the material changes. Instead, φ_{eff} is a

corrected value such that the material strength is equivalent to that of a material with an intrinsic internal angle of friction, φ, and a pore pressure, P_f (equation 2).

Effect of Deformation on the Strengths of Faults and Shear Zones

The strengths of faults and shear zones is controversial, and they have been interpreted to be either much weaker (e.g., Chéry et al., 2001; Provost and Houston, 2003), or of similar strength (e.g., Scholz, 2000) to adjacent relatively non-deforming regions. We acknowledge that faults may be weak, note mechanisms that may produce weak faults and shear zones, and describe a simple parametric representation of these processes which we use in the numerical models.

Deformation can result in changes in material strength. Fracturing of intact rock leads to a reduction in cohesive strength, but this reduction may not be significant because the bulk cohesion of undeformed rocks at the 1-10 km vertical scale of our models may be an order of magnitude less than that of unfractured laboratory samples due to the near-ubiquitous presence of natural fractures and joints (e.g., Schultz, 1996). At the scale of the crust, the dominance of the pressure-dependent term in equation 1 means that changes in φ_{eff} with strain may strongly affect structural development. Materials may strain-harden (φ_{eff} and $\sqrt{J_2'}$ increase) or strain-soften (φ_{eff} and $\sqrt{J_2'}$ decrease), perhaps due to a transient decrease or increase in pore fluid pressure, respectively, or other less well constrained mechanisms that instead change the intrinsic rock properties. For example, mineral transformations that occur during the formation of gouge reduce φ with increasing deformation and can result in a large frictional strength reduction, (e.g., φ = 10° – 3° for mica-rich gouge; Bos and Spiers,

2002). Although these various mechanisms require more investigation, we can determine their potential effects in model sensitivity experiments by including a very simple parametric form of strain-dependent weakening. Strain softening is introduced by a linear decrease of $\varphi_{eff}(\varepsilon)$ over a range of strain (here, $0.5 < \varepsilon < 1.0$), where ε represents the second deviatoric strain invariant, $\sqrt{I_2'}$. Strain softening is not required for strain localization in the model experiments because we use a non-associative flow law. However, as we demonstrate below, strain softening has significant effects on the model results.

Mechanical Model Description

We use an Arbitrary Lagrangian-Eulerian (ALE) finite element method for the solution of mechanically coupled, plane-strain, incompressible viscous-plastic creeping flows (for details see Fullsack, 1995, Willett, 1999, and Huismans and Beaumont, 2003), to investigate deformation of a layered sedimentary system with frictional-plastic materials. The ALE formulation allows computation of large-deformation, plane-strain flows in a vertical cross-section, subject to velocity boundary conditions applied to the model boundaries. Although the FE code is capable of modelling coupled mechanical and thermal evolution, and the consequences for temperature-dependent rheologies (e.g., Beaumont et al., 2004), we do not consider thermal aspects here, as noted above. The velocity and deformation for the whole model domain are calculated dynamically, in response to kinematic velocity boundary conditions (Figure 2). The FE solutions are determined using a variational formulation that minimizes viscous dissipation (i.e., they are minimum rate of work solutions).

The plastic strain and associated deformation are modelled as an incompressible viscous flow, where the effective viscosity is dynamically adjusted for those regions that are on the verge of frictional-plastic yield such that they remain on the failure envelope (Fullsack, 1995; Willett, 1999). The effective viscosity for plastic flow, η_{eff}^{P}, is:

(3) $$\eta_{eff}^{P} = \tfrac{1}{2}\sqrt{J_2'} \Big/ \sqrt{\dot{I}_2'} .$$

Setting the viscosity to η_{eff}^{P} for regions that are on the verge of failure satisfies the yield condition (1) and allows the velocity field for viscous creeping flow to be determined iteratively through a FE approach. For regions that are not on the failure envelope (i.e., "rigid"), the effective viscosity is many orders of magnitude greater (10^{30} Pa s), sufficiently high that negligible deformation occurs on the model timescale.

The velocity and deformation calculations are performed on an Eulerian FE grid that is fixed horizontally with respect to an external reference frame, but stretches vertically as the material deforms (Fullsack, 1995). A cloud of Lagrangian tracer particles and an associated Lagrangian mesh, which are advected with the deforming material, allows tracking of material types and properties, and is used to incrementally update these properties on the Eulerian grid. The initially uniform rectangular Lagrangian mesh provides a convenient visual representation of strain variation within the deforming wedge. In figures below, a simplified representation (showing every third mesh line, horizontally and vertically) of the Lagrangian mesh is shown as hairlines overlying the Eulerian grid, which is coloured according to material type.

The initial Eulerian grid for all models presented here has dimensions of 200 km by 5 km and encompasses 800 by 78 elements (horizontally and vertically, respectively). Neither the number nor the horizontal positions of Eulerian elements

changes during a model run, and therefore the initially elongate elements (each 250 m by approximately 64.1 m at the start of each model) are subsequently stretched vertically to sub-equal dimensions. At the start of each model, prior to deformation, the Eulerian and Lagrangian meshes overlie each other identically. However, the Lagrangian mesh is four times the width of the Eulerian grid in horizontal extent (800 km) and element number (3200), to allow for material to be carried into the Eulerian grid during model convergence (Figure 2, Table 1).

As noted above, material is introduced into the Eulerian grid on the right-hand side of the models, carried at constant velocity on the model base. The convergence rate for all models presented here is 10 mm/year. Each model time step is 1,250 years, equivalent to 12.5 m of convergence (5% of the Eulerian element width). One million years of model evolution is therefore represented by 800 time steps.

Surface Processes

There is a growing literature addressing the computational aspects of coupled tectonics and landscape evolution (e.g., Braun and Sambridge, 1997; Willett et al., 2001), and how it may relate to regional climatic variables such as orographic rainfall distributions (e.g., Beaumont et al., 2000; Roe et al., 2003). Here, however, we model surface processes using very simple, first-order approaches. Our intention is to demonstrate the degree to which even the simplest surface process models can influence structural style.

For erosion, we use a linear, slope-dependent model where the rate of erosion at a given surface node location is directly proportional to the surface slope, calculated from the average of the slopes of the current Eulerian grid in the two adjacent surface

elements. Here, for simplicity, we use a spatially constant erosion rate equal to 1 mm/year on a 1:1 (45°) slope. More complex, spatially and temporally variable models are easily incorporated, but are not justified at the present level of study.

For sedimentation, we consider simple end-member states, where there is either no significant sedimentation, or where sediments completely fill available accommodation space up to a specified base level. Here, we choose the base level to be the initial upper free surface of the model layers prior to any shortening. In the case of no significant sedimentation, very minor sedimentation can occur in the cores of very tight synclines, as a consequence of the vertical re-gridding of the Eulerian grid.

Note that because the rheologies in Table 2 are all plastic and therefore rate-independent, the erosion rate and the convergence rate can be scaled together. For example, a model result for a convergence rate of 10 mm/year and an erosion rate of 1 mm/year (on a 1:1 slope) will be identical to that for a convergence rate of 1 mm/year and an erosion rate of 0.1 mm/year, assuming all other parameters are equal. Under these circumstances only the elapsed time differs among the scaled models, the timescale increasing with decreasing convergence rate and erosion rate.

Model Results

We present a series of eight models that progressively increase in complexity (Table 2). In our FE approach, the material within the wedge is a continuum. Therefore, there are no discrete faults although narrow zones of very high shear strain develop that emulate faults, resulting in thrust-and-fold belt-like features. In our descriptions of these features, it is sometimes easiest to use terminology typical of thrust-and-fold belts,

including calling the narrow shear zones “thrusts” that bound “thrust sheets”. However, this is merely for convenience, and the distinction should not be forgotten. It is also important to remember that the internal angle of friction and cohesion are initially uniform in each of the model layers. No lateral discontinuities or other special effects are used to initiate or control the localization of deformation.

In all model figures, every 20th vertical line in the illustrated Lagrangian tracking mesh is a bold line for ease of visual reference, and is labelled with a sequential number. These bold vertical lines are initially spaced 15 km apart. The numbers vertically overlie the upper ends of these lines, immediately above the active surface of the model, regardless of whether portions of the Lagrangian mesh are removed by erosion, or overlain by later sediment. In practice, this can result in the number labels becoming transposed where significant overthrusting or in-folding occurs.

Model 1

Model 1 (Figure 3) is an example of the simplest case of a one-detachment configuration (Figure 2) where the wedge base is horizontal and does not respond isostatically. The strong overlying layer has an effective angle of 38° (a typical “dry” value, with no pore fluid pressure, comparable to an analogue “sandbox” experiment), whereas the weak basal detachment has an effective angle of internal friction of 3.5° (which can be interpreted to correspond to very high pore fluid pressures; equation 2), resulting in an effective strength ratio of 10:1 (Table 1). There is neither erosion nor sedimentation (Table 2).

The mode of deformation within the wedge, characterized by triangular pop-up structures, is significantly different from that proposed by Dahlen and Suppe (1988) and

Dahlen and Barr (1989), in which quasi-pure shear strain is specified to maintain an exact, uniformly dipping upper wedge surface. These pop-up structures, bounded by discrete high-strain shear zones ("faults"), are similar to those observed in analogue experiments (e.g., Lui et al., 1992). However, in Model 1 there is no strain dependence of the material properties, unlike the sand and other materials used in analogue experiments which initially strain harden and then strain soften according to the initial packing of the granular material. Therefore, localized deformation is not simply a consequence of strain-dependent material properties.

The shear zones resemble slip-lines in ideal rigid-plastic materials (e.g., Hill, 1950), which are the characteristics of the hyperbolic equilibrium equations. As noted above, the ALE FE formulation produces minimum rate of work solutions. This suggests that although quasi-pure shear solutions are admissible, they may not be minimum work solutions and are therefore not selected as the FE mode of deformation. Alternatively, it is clear from the model result that the size of the pop-up structures scales with the thickness of the undeformed layer, and these occur because the wedge is grown from a finite thickness layer. Such pop-ups have no equivalents in critical wedge mechanics because the wedge is assumed to have a self-similar geometry and is not 'grown' from a uniform layer.

As model 1 grows, the nearly regular nature of newly developing pop-up structures is occasionally interrupted, as at 4.5 My, between marker numbers 7 and 9 (Figure 3c). This deviation is probably a numerical artefact because models with more stringent convergence requirements, and therefore more iterations per time step, exhibit a more regular progression. The regular pop-up pattern across this segment of the

wedge is also largely restored by 6.0 My (Figure 3d). The wedge subsequently begins to self-organize into larger, discrete thrust sheets, generally consisting of two adjacent pop-up structures and the underlying intervening triangular regions. This pattern and its development are seen at 12 My and earlier times, where the thrust sheets are being carried on “faults” that intersect the surface near markers 5, 9, 12, and 16 (Figure 3h). This self-organization and localization of strain occurs in the absence of strain-softening or strain-hardening. In some cases, the maintenance of localized high shear strain, in the absence of strain-softening or hardening, may be due in part to the advection of small amounts of weak material into the shear zones.

For effective friction angles of 38° and 3.5° for the wedge and the thin basal layer, respectively, and a horizontal base, the upper surface slope predicted by the cohesionless wedge theory of Dahlen (1984) is 0.835° (the 2 MPa cohesion is negligible in comparison to wedge strength, except very near the surface). By comparison, the average slope of Model 1 depends on the way the slope is measured: it is approximately 1.6° if the tangent to the top of the pop-ups is used, but very close to the predicted value if the line through the minimum heights is used (Figure 3, part 1). We suggest the latter is the correct estimate and that topography above this minimum line makes these thicker regions of the wedge supercritical. It is the minimum heights that must reach the critical slope line in order that the wedge attains an overall critical state and can translate without further internal deformation. Small deviations of the minimum heights from the critical slope line near the rear of the wedge probably reflect slight weakening of the bulk wedge strength due to the advection of weak basal material upward into the wedge along the growing shear zones.

Most structures initiate in an “in-sequence” fashion, but can remain active or be episodically active for protracted periods. Strain-rates and velocities (not shown for this model, but see Model 8, below) indicate shifting patterns of deformation where large segments of the wedge may be sliding passively while strain is localized in shear zones bounding one or more pop-up structures. However, all structures must be periodically reactivated, or equivalent new structures created, in order that the wedge can shorten and thicken in an overall self-similar manner. Out-of-sequence thrusting is therefore required to maintain overall uniform taper.

The surface of the model, although not “eroded” as in other models below (Table 2), is subject to minor smoothing due to the numerical filtering that occurs because the finite elements have a finite width (in this case 250 m), and therefore cannot represent shorter scale topographic variations. A consequence of this approach is the numerical infolding of very small volumes of material in the cores of synclinal structures where the top of the Lagrangian tracking mesh has been folded beneath the top of the Eulerian mesh at a length scale shorter than the finite element width. This material, which appears as “sediment” (e.g. Figure 3g), is assigned properties identical to the underlying layer (Table 1).

Model 2

Model 2 is identical to Model 1 except that the base of the model responds isostatically to wedge thickening (Figure 4 and Table 2). The base behaves like a uniform, thin elastic plate with a flexural rigidity of 10^{23} Nm, equivalent to an effective elastic thickness of approximately 25 km (assuming a Young’s modulus of 70 GPa and a Poisson’s ratio of 0.25).

The pattern of self-organization into pop-up structures that amalgamate to form thrust sheets is again produced. For example, at 18 My there is a semi-regular pattern of thrust sheets carried on faults that intersect the surface near marker numbers 8, 10, 13, 16, 18, and 20 (Figure 4f). By following the development of these features both backward and forward in time, the pattern of self-organization becomes apparent. The narrow zones of instantaneous high shear strain are not fixed with respect to the wedge material, but may move as the wedge thickens and adjusts isostatically. This can result in broad zones of the Lagrangian mesh characterized by moderate to high total shear strain, as seen intersecting the surface at 24 My near markers 8, 14, 19, and 23 (Figure 4h).

In Model 2 the overall wedge taper angle is larger than in Model 1 owing to isostatic adjustment and the increase in basal slope. Achievement of this larger taper angle requires larger internal strain, which leads to enhanced self-organization and amalgamation of the pop-up structures into thrust sheets noted above (compare Figures 3f and 4f which both have similar wedge toe positions). This process illustrates two features of the deformation that lead to the development of internal structure resembling that of natural TFBs. Both features also lead to departures from the uniform taper predicted by critical wedge theory.

The first feature is the length-scale of the pop-ups, which is determined by the finite thickness of the layer accreted at the wedge toe. The effect of accretion of a finite-thickness layer is not explicitly considered in critical wedge existence theories. The second feature is the amalgamation of pop-ups into thrust sheets, which we speculate occurs because the thickness of the interior of the wedge is too large to be compatible

with deformation that occurs on a scale determined by the size of the initial pop-ups. The system must either select new, correspondingly larger pop-up length-scales for the interior of the wedge, or scale up of the sizes of the deformation units by amalgamating groups of pop-ups. In Models 1 and 2 the latter choice occurs, possibly because the minimum dissipation solution is also conditioned by the wedge geometry and detailed surface topography which are influenced by the initial geometry and length-scale of pop-up deformation.

Model 3

Model 3 is similar to Model 2, but with the addition of a second, internal, detachment horizon, resulting in a 2-detachment configuration (Figures 2 and 5, and Table 2). This internal detachment is weaker (φ_{eff} = 1°) than the basal detachment (φ_{eff} = 3.5°) leading to an effective strength ratio of 0.28:1 between the two (Table 1). With these properties and φ_{eff} = 38° for the two equal-thickness strong layers, the basal décollement, which underlies the deforming wedge, steps up from the model base to an intermediate level, as in the archetypal SCRM (Figure 1). In SCRM terms, the two-detachment model can be viewed as being broadly similar to the thick and relatively strong Mesozoic foreland clastics overlying the thin and weak Fernie Formation (principal detachment 2, Figure 1), in turn overlying thick and strong Paleozoic carbonates above a weak basal detachment overlying the crystalline basement (principal detachment 1, Figure 1), although this simple view of the SCRM is complicated by secondary detachments within both the carbonate and clastic-dominated sections.

The inclusion of the internal detachment dramatically influences the structural style, leading to longer thrust sheets in the lower strong layer along with associated fault-bend folds and duplex structures. There is a tendency for the models to produce break-thrusts and “snake head” structures at the leading edges of these lower-layer thrust sheets (e.g., at 9 My between markers 10 and 11, Figure 5c), and to internally thicken during transport in a series of pop-up structures (e.g., at 18 My between markers 16 and 18, Figure 5f).

The trajectory of the basal décollement adopts two basic forms during model evolution. The first involves the décollement stepping up from the basal detachment horizon to the intermediate detachment level a significant distance back from the toe of the wedge. Well-developed examples are seen at 9 My and 12 My (Figure 5c and 5d). Alternatively, the décollement can lie within the basal detachment horizon essentially to the toe of the deforming wedge, as seen at 6 My (Figure 5b), and at 15 My and later (Figure 5e–h). That these two forms develop, in spite of there being no change in the material strengths of the basal and intermediate detachments, implies that the detailed internal deformation pattern is responding to geometrical changes in material distribution within the wedge and possibly to changes in the basal slope across the model. In addition, although the model TFB has an overall wedge shape (Figure 5), there are significant sub-wedge-scale departures from the uniform taper predicted for critical Coulomb wedges.

Model 4

Model 4 (Figure 6) is identical to Model 3 except that the two thick strong layers undergo strain-softening (Table 2). They are initially as strong as the thick layers in

models 1 through 3, but φ_{eff} decreases linearly from 38° to 18° (a 50% decrease in strength; Table 1) over a narrow strain range of 0.5 to 1.0 (strain magnitude is equated to the second invariant of the deviatoric strain tensor). There is little sensitivity of model results to the upper limit of the strain softening range, because strain-softening leads to strong positive feedback and increased focusing of strain. The strain-softened value of φ_{eff} =18° value could be viewed either as a consequence of localized, moderate pore fluid overpressures (equation (2)), with a λ value of 0.50 (equivalent to a λ_{HR} value of 0.72; see Appendix and Table 1), or as a consequence of material strain-softening of major fault zones which occurs in nature through a variety of mechanisms, as discussed above.

Model 4 develops very differently than does Model 3. The primary difference is the contrasting deformation styles in the upper and lower strong layers, both of which undergo equal strain softening. The upper layer develops relatively short thrust sheets with less backthrusting than the equivalent structures in Model 3 (Figure 6c-h). These structural units are very similar to the thrust sheets seen in Models 1 and 2, which derive from the amalgamation of four pop-up structures, except in this case the amalgamation occurs before there is substantial deformation between the pop-ups. These thrust sheets undergo less internal shortening during transport than in Model 3, due to feedback-facilitated, strain-softening strain localization and strength reduction within shear zones that cross-cut the strong, little-strained layers.

In contrast, very long thrust sheets develop in the lower strong layer, as seen at 18 My and 24 My (Figure 6f and 6h), which more closely resemble structures in natural systems. These long thrust sheets are also transported large distances, equal to a

significant fraction of their length, with little internal deformation. Stacking of the lower thrust sheets gives the wedge a large-scale swell-and-dip surface morphology (Figure 6d and f). These long thrust sheets are generally dismembered later in the model evolution by localized, out-of-sequence structures. For example, compare Figure 6f with Figure 6g: out-of-sequence faults are localized above a footwall ramp beneath markers 13 and 14, Figure 6g. There is also a tendency in Model 4 for the basal décollement to cut up through the lower strong layer to the intermediate level detachment a significant distance behind (toward the backstop) the deformation front in the upper layer, similar to the SCRM archetype (Figure 1).

Model 5

Model 5 (Figure 7) is identical to Model 4 except that the upper surface is subjected to significant erosion (Table 2). As noted above, we use a simple model where erosion rate is a linear function of local surface slope, with a rate of 1 mm/year on a 1:1 slope, which equates to 0.1mm/year on a 1:10 slope. Eroded material is removed from the model.

Comparison of Model 5 (Figure 7) with Model 4 (Figure 6) shows that the effect of erosion is primarily to reduce the total volume of the wedge at any given time, with a concomitant effect on the details of the structure, but not to change the overall structural style markedly. However, one clear though minor influence on structural style is the enhancement of the pop-up structures that develop at the leading edges of short thrust sheets within the upper strong layer. This is an inferred model example of positive feedback between structures and surface processes. Wherever there is active shortening within the wedge that results in an increase in surface slope, there is an

associated increase in erosion rate that in turn results in a focusing of additional shortening.

Model 6

Model 6 (Figure 8) is similar to Model 5 except that rapid sedimentation results in the filling of all accommodation space below base level at each time step (Table 2), with material that has the same mechanical properties as the upper strong layer (Table 1), and which is fully involved in the deformation of the wedge. Although the syndeformational sediment is not overlain by the initial Lagrangian tracking mesh (Figure 8), it is fully tracked during deformation for re-gridding onto the Eulerian grid. For ease of display, the colour of sedimentary strata is changed every 2 My, and the pattern repeats after five cycles (every 10 My). No attempt is made to balance the volume of sediment against that removed by erosion. In nature, the region we are modelling would be part of a much larger system, with significant potential sediment sources in the hinterland as well as along strike. In Model 6, the onset of sedimentation and erosion is delayed until 4.5 My, to allow the model to develop the initial buffer wedge as explained above (in Model 5, erosion begins at 0 My).

The influence of syndeformational deposition on model structural style is profound. As the foreland basin deepens in Model 6, the deformation front (wedge toe) steps out into the foreland a distance several times the thickness of the wedge. This pattern is repeated as the wedge evolves (Figure 8). As the model base isostatically subsides due to growth of the wedge, the slope of the base increases. In combination with active sedimentation in front of the deforming wedge (in the foreland basin), this episodically results in achievement of overall critical or supercritical taper of the foreland

basin out to the nascent wedge toe without the requirement of internal shortening. This process results in an abrupt forward step in the position of the deformation front and the incorporation of the proximal region of the foreland basin into the wedge as an initially undeformed piggyback basin (Figure 8d, e).

As convergence continues, shortening across the wedge tends to concentrate in the more highly strained regions flanking the piggyback basin, probably encouraged by the positive feedback effect of slope-dependent erosion and further deposition of sediments in the piggyback basin which respectively weakens and strengthens these regions. Weakening is also enhanced by the strain softening of the two thick layers that follows soon after the onset of their deformation. With further shortening, the cycle that forms piggyback basins tends to repeat itself, resulting in a structural style where broad, relatively little deformed synclinal areas are separated by significantly more deformed anticlinal structures (Figures 8f, g, h).

In effect, the coupling of wedge growth to sedimentation allows the system to bypass the deformation required for the constructional phase of wedge taper development, and move directly to a state where at least part of the wedge has a critical or supercritical taper (i.e., translating on the basal décollement, but with effectively no internal strain). For example, the tapers of the frontal portions of the wedges, detached on the weak internal detachment, are very similar in Figure 8d and Figure 7c-h. However, this taper was achieved in Model 5 through internal shortening (the constructional phase), whereas in Model 6 critical taper developed due to sedimentation in an asymmetrically subsiding foreland basin.

Similar to the structural evolution of Models 4 and 5, the basal décollement of Model 6 cuts up through the lower strong layer, to the intermediate level detachment, a significant distance behind the toe of the wedge (Figure 8). When the basal décollement jumps forward and down-section to incorporate a slice of the strong lower layer into the wedge, the leading edge ramp through this layer is located significantly toward the hinterland of the current toe of the wedge but is more closely aligned with the penultimate wedge toe (see labelled ramps and wedge toes in Figure 8e and 8f). As contraction continues, a number of out-of-sequence structures cross-cut and shorten the piggyback basins (examples labelled in Figure 8f–h). Some of these structures are related to the forward jumps in the basal decollement.

Model 7

Model 7 (Figure 9) is similar to Model 4, except that a second internal detachment layer is introduced, resulting in a 3-detachment model configuration (Figure 2, Table 2). As in the previous cases, the two internal detachment layers are weaker than the basal detachment layer and the thick strong layers undergo strain softening (Table 1). In SCRM terms, the three-detachment model can be viewed as being broadly similar to those areas where in addition to a regional detachment in the Fernie Formation, between the thick and strong Paleozoic carbonates and the Mesozoic foreland succession, there is a regional detachment within the Upper Cretaceous marine shales.

The introduction of a second internal detachment leads to structural geometries similar to those in the simpler 2-detachment models, but they have elements even more reminiscent of natural TFBs. For example, Model 7 shows well-developed flat-ramp-flat

geometries of the basal and internal decollements, and associated fault-bend folds, duplexes, and antiformal stacks. Except for the uppermost strong layer, which deforms into a series of short imbricate thrust sheets, the thrust sheets are commonly very long relative to their thickness and are little deformed internally, except near their leading edges. The contrast in the deformation style of the two upper strong layers is particularly significant because these layers have the same properties as do their underlying detachment layers. Evidently, layers with the same properties can behave quite differently depending on their depth in the system (because they experience different pressures), and on their positions relative to other weak and strong layers (middle layer is confined below another strong layer, whereas the top layer is not).

The long thrust sheets, composed of slices of the middle strong layer, are accreted to the base of the growing wedge. This basal accretion occurs beneath a shallow-based deforming wedge composed of tight imbricate slices of the upper strong layer (for example, compare Figure 9e with 9f). The progressive stepping out of the basal décollement, toward the foreland in a flat-ramp-flat fashion, leads to a characteristic geometry of a series of anticlinally folded thrust sheets, cored by the thickened leading edges of basal layer thrust sheets, whose structural elevation increases steadily toward the back of the wedge (Figure 9h).

Model 8

Model 8 (Figure 10) is the same as Model 7, except it is subjected to both surface erosion and rapid deposition below base level (Model 8 is to Model 7 as Model 6 is to Model 4; Table 2). As in Model 6, sedimentation and erosion begin at 4.5 My, to allow the model to develop an initial wedge and form the hinterland edge of the evolving foreland basin, and sediments are coloured in a cyclic fashion for display purposes.

As seen in Model 6, syndeformational deposition has a profound influence on structural style. As the wedge evolves, the wedge toe repeatedly steps out a substantial distance into the foreland, with the intervening segment of the wedge being transported with little or no internal strain. This distance is respectively larger or smaller when either the upper two strong layers detach together (Figure 10b, e), or only the uppermost layer detaches (Figure 10d, f). Concurrent erosion and deposition lead to development of out-of-sequence thrusts (Figure 10d, g) as well as on-lap of piggyback basin strata across the leading edges of formerly active and eroded thrust sheets (Figure 10f–h). These relationships illustrate the structural complexity that can develop due to feedback between surface processes, even very simply implemented, applied to geometrically simple initial material geometries (Figure 2).

Figure 11 shows instantaneous velocities and strain-rates for Model 8. Velocity vectors are shown relative to the backstop, and demonstrate that deformation patterns vary across the wedge in time as well as space. Shortening and uplift can be concentrated at or near the toe of the wedge, as in Figure 11a, 11b, 11e, or 11h, or internally, with the toe being nearly passively transported, as in Figure 11c, 11d, 11f, and 11g. This spatial variation in velocities is mirrored by the strain-rate magnitudes. In

addition, the strain-rates show how large regions of the model undergo little to no instantaneous strain as they are passively transported.

Discussion

Comparison to Natural Structures and the Importance of Surface Processes

The four characteristics of thin-skinned thrust-and-fold belts noted by Chapple (1978) are essential features at whole-wedge scales. However, the pattern of internal strain implied by whole-wedge models (e.g., Stockmal, 1983; Dahlen and Suppe, 1988; Dahlen and Barr, 1989) is akin to pure shear shortening and does not allow details of natural thrust-and-fold belt structures and styles to be used effectively as constraints on model parameters. Although many details are specific to particular thrust-and-fold belts, some generalizations regarding sub-whole-wedge characteristics are possible, as exemplified by the SCRM (Figure 1). These include: (1) the presence of discrete thrust sheets with relatively little internal shortening and relative displacements on the order of the wedge thickness or greater, (2) an overall sense of structural vergence, directed toward the foreland, although this can vary markedly in degree from belt to belt, (3) multiple detachment levels resulting in ramp and flat geometries and associated structures (e.g., folded thrust sheets, duplexes, antiformal stacks), and (4) a progressive stratigraphic shallowing of the basal decollement toward the foreland and the toe of the wedge, facilitated by the multiple detachment levels. These features should be essential elements of any viable thrust-and-fold belt model, whether numerical or analogue, intended to address sub-whole-wedge structure. The dynamical models presented here,

especially those with multiple detachment levels, clearly display the above sub-whole-wedge characteristics.

In addition, many thrust and fold belts contain syndeformational piggyback basins, but typical basins of this type are not observed in the archetypal SCRM (Figure 1), which raises the question whether the SCRM are more like Models 5 and 7, without piggyback basins, or whether such basins have been eroded. A particular characteristic of Models 6 and 8 is broad relatively little-deformed synforms at lower levels in the piggyback basins, separating narrower more heavily shortened antiformal structures. This general structural style of antiforms and synforms is reminiscent of eroded features observed in the Foothills of the SCRM and elsewhere.

Figure 12a is a cross-section across the eastern Front Ranges and the Foothills of the SCRM, 100 km northwest of Calgary, Alberta (after Ollerenshaw, 1978). The Sheep Creek, Burnt Timber, Williams Creek, and Grease Creek synclines comprise a series of broad, relatively little deformed synforms (the Grease Creek Syncline is virtually unfaulted 10 km to the south). Although the magnitude of post-deformational erosion across the Alberta Foothills is sufficiently large (2 to 5 km or more; e.g., Osborn et al., in press) that direct syndeformational sedimentological evidence has been removed, comparison of these synformal structures to those of models 6 and 8 suggest that they may mark the keels of now-eroded piggyback basins. The Alberta Syncline, which overlies a blind triangle zone at the edge of the Foothills, may also owe its existence to feedback between surface processes and structural development (Stockmal et al., 2001).

Figure 12b is a cross-section modified after Mountjoy et al. (2002) that extends across the eastern edge of the Front Ranges and most of the Foothills belt, approximately 250 km northwest of Calgary, Alberta. A series of synclines is observed (Bighorn, Black Mountain, and Brazeau synclines, and an unnamed syncline in the hanging wall of the Ancona Thrust, AT) that are progressively more structurally uplifted to the west. Again, the influence of syndeformational sedimentation on structural style observed in Models 6 and 8 suggests that these broad synforms may mark the axes of now-eroded piggyback basins.

Figure 12c is a cross-section from Ramos et al. (2004), across the Sub-Andean belt, northern Argentina. The broad synclines are occupied by synorogenic sediments that document a complex pattern of development. Although there is an initial overall foreland-breaking sequence for the main faults, there is clear sedimentary evidence of out-of-sequence and simultaneous motion on a series of thin-skinned thrusts (Ramos et al., 2004). Similar, less eroded, features are observed near the leading edges of other orogens, both active and inactive (e.g., Ori and Friend, 1984; Pinvik and Khan, 1996; Leturmy et al., 2000).

The intimate relationship between thin-skinned thrusting and syndeformational sedimentation is well illustrated by Pieri (1989) in a series of spectacular seismic lines across the Po Plain, adjacent to the Apennines. Figure 13a is a portion of his seismic line B-B', showing thrusted Paleogene and Miogene sediments, partly eroded and onlapped by Pliocene and Quaternary deposits, which are in turn slightly deformed. For comparison, Figure 13b and 13c show portions of Model 8 (Figure 10g and 10h) where similar relationships have evolved. A formerly emergent thrust toe, cut off by an out-of-

sequence trailing imbricate, is progressively onlapped and buried by the piggyback basin. These sediments are in turn slightly deformed during later minor motion on the pre-existing thrust faults.

Although the initial formation of model thrust faults is generally in an in-sequence fashion, with those faults lying more toward the foreland being younger, many of the model faults are long-lived or are continuously reactivated, and some form as out-of-sequence features (as illustrated in Figure 11). Commonly, balanced cross-sections are constructed assuming not only an in-sequence development, but with all fault motion essential complete prior to motion on the next thrust; however, basic critical wedge concepts and the FE models indicate that these assumptions must be overly simplistic. Although out-of-sequence or simultaneous motion in the SCRM is not obvious in Figure 1, Price (2001) has argued that map-scale relationships require simultaneous or temporally overlapping motion on a series of thrust faults in the Front Ranges, and palinspastic reconstruction suggests out-of-sequence motion on the McConnell thrust through the Mesozoic section (Price and Fermor, 1985). Models 6 and 8 suggest that such out-of-sequence features may be intimately related to feedback with surface processes.

Surface processes, and in particular, syndeformational sedimentation, are essential components of the TFB system. Feedback between these processes and structural style can be profound, as seen in the differences between models 4 and 6 (Figures 6 and 8) and between models 7 and 8 (Figures 9 and 10). Much of the regularity observed in TFBs, including spacing of major thrust faults in palinspastic

restoration, may owe its existence to dynamical feedback within the overall mechanical system.

Comparison to Whole-Wedge Solutions

The dynamical models develop *overall* wedge shapes that are broadly consistent with the critical wedge geometries predicted by Chapple (1978), Davis et al. (1983), and Dahlen (1984), among others, although there are significant departures from “ideal” critical wedge shapes. Of course, the details of such departures in natural orogens, both in external shape and internal form, provide much of the inspiration and motivation to structural geologists working in TFBs. They are the problem to be solved. The closed-form solutions of these authors, especially that of Dahlen (1984), have been applied to natural orogens, usually to constrain one (or more) unknown variable, such as the internal coefficient of friction, basal coefficient of sliding friction, or the internal or basal pore fluid pressure ratio (e.g., Dahlen, 1990). The values derived by this approach are appropriate at the scale of the natural wedge assuming that the underlying assumptions are valid, but they are unlikely to be representative of structures at smaller scales. This applies to material strengths and pore pressure values, as well as velocity or strain distributions.

Our dynamical numerical models imply that décollements underlying large thrust sheets are very much weaker than the thrust sheets themselves (see next section below). When this is not the case, model thrust sheets (unpublished models) shorten internally far more, and are translated far less, than commonly observed in nature in the external portions of TFBs. In contrast, although bulk internal wedge strength must of course be greater than basal strength, their ratio derived from whole-wedge solutions

(e.g., Davis et al., 1983; Dahlen et al., 1984; Dahlen, 1984, 1990) is typically much smaller than the ratios of strong to weak materials in our numerical models that reproduce “realistic-appearing” structures. This discrepancy may reflect the “averaging” of material properties necessary at whole-wedge scales: the average strength of the basal décollement may be somewhat greater than the local strength within a particular detachment due to the décollement episodically ramping up through stronger layers. Similarly, the average strength of the wedge will probably be significantly less than the local strength within an intact thrust sheet due to the presence of much weaker detachments and strain-weakened shear zones throughout the wedge.

For example, for Model 8, the average whole-wedge surface and basal slopes at 12, 15, and 18 My are 1.86°, 1.47°, and 1.19°, and 5.82°, 3.96°, and 4.09°, respectively (Figure 14a), where slopes are derived from least-squares linear fits to equally-spaced points along the surfaces bounding the deformed wedges. Corresponding values of the internal friction within the wedge, $\varphi_{eff,}$ and sliding friction on the base, $\varphi_{b,eff,}$ derived from the equations of Dahlen (1984) and consistent with these whole-wedge average slopes, are shown for each of these time steps in Figure 14b, as solid lines labelled “W-W”. In the plots shown in Figure 14b, the range encompassed by the weak detachment values, 3.5° and 1°, is indicated by the shaded horizontal bar, and the range of possible values of the strong, strain-softening layers, from 38° to 18°, is encompassed by the broad, stippled vertical box. Note that none of the whole-wedge solution curves pass through the area formed by the overlap of these two zones.

Also shown in Figure 14a are local slopes (indicated by dotted lines). The local upper surface of the wedge is derived by fitting a straight line by eye to topographic low

points, similar to the approach illustrated for Model 1 where the Dahlen (1984) solution was seen to essentially match the FE solution. The local basal surface is the average dip on the décollement where it is confined to the very gently curving detachment layers. Local slopes were determined at the wedge-front (W-F) for all three time frames in Figure 14 and at the wedge-middle (W-M) for the 15 and 18 My frames. Local slope values are enclosed in parentheses in Figure 14a.

As seen in Figure 14b, the curves of $\varphi_{b,eff}$ versus φ_{eff} for all three wedge-front regions intersect the area of overlap between the ranges of model effective friction angles for the strong thick layers and the weak detachments. However, none of these curves has an acceptable solution for $\varphi_{b,eff}$ equal to 1°, which is the appropriate basal effective friction angle at the wedge fronts, where the wedges are detached on one or the other very weak internal detachment layer. This discrepancy between the FE model and the Dahlen (1984) solution may be due either to the accretion of a finite-thickness layer at the wedge toe, which is not explicitly considered by Dahlen (1984), or it may reflect the fact that each of these regions may be largely or at least partly supercritical at these time frames, as implied by the velocity and strain-rate distributions shown in Figure 11. The curves of $\varphi_{b,eff}$ versus φ_{eff} for the wedge-middle regions for the 12 and 15 My time frames (Figure 14b) are either nearly coincident with the whole-wedge curve (12 My) or above it (15 My).

If we assume, simply for discussion, that the average or whole-wedge strength of the basal décollement, which is localized within detachment horizons with effective angles of internal friction of 3.5° and 1°, lies at the upper extreme, i.e., 3.5° (perhaps reflecting the brief cross-cutting of stronger layers), then Figure 14b (circles) shows that

for this value of $\varphi_{b,\text{-eff,}}$ the maximum value of φ_{eff} is approximately 6 to 11°. This whole-wedge value can be interpreted to indicate the minimum degree to which both the weak internal detachments and the strain-weakened shear zones contribute to the bulk strength of the entire wedge.

Using equation (2), we can express φ_{eff} in terms of pore fluid pressure. If we assume an angle of internal friction of 38° for sedimentary rocks, then the pore fluid pressure ratios ($\lambda = P_f / P$) required to reduce the whole-wedge effective angle of internal friction to 6 to 11° are 0.83 to 0.69, respectively. Using equation (A10), these values expressed in terms of the familiar Hubbert-Rubey pore pressure ratio, λ_{HR}, are 0.927 to 0.853, respectfully. Similar pore pressure ratios were derived by Davis et al. (1983), Dahlen et al. (1984) and Dahlen (1984, 1990) for some deforming wedges (particularly accretionary wedges). Excess pore pressure values are widely observed in tectonically active and inactive TFBs and associated basins, and undoubtedly contribute to the weakening of rocks in the brittle domain. However, because very weak faults internal to the wedge are not explicitly accounted for in whole-wedge solutions, pore pressure ratios derived from these solutions are likely to overestimate natural values.

Similarly, the nature of internal deformation implied by the whole-wedge models (e.g., Dahlen and Barr, 1989), although consistent with their evolution at the scale of the entire wedge, are not particularly useful at smaller scales. This has implications for the determination of mechanical energy budgets, and assessment of TFB evolution through minimum work arguments. For example, compare the whole-wedge results of Dahlen and Barr (1989) to the sub-whole-wedge-motivated approaches of Mitra and Boyer (1986), Hardy et al. (1998), Masek and Duncan (1998), and Cooke and Murphy (2004).

Numerical model departures from ideal wedge shapes not only reflect the details of how different strength materials are distributed within the wedge, they also reflect the fact that large portions of the wedge are not at yield but are being transported passively with essentially no internal strain. This is most evident in models involving syndeformational deposition (Models 6 and 8). Flexural subsidence and foreland deposition can result in development of a critical or supercritical wedge segment, effectively bypassing the internal deformation commonly associated with the constructional phase required to produce a critical taper. If the taper of a wedge beneath a piggyback basin (incorporated as a consequence of a large step in the position of the deformation front) is supercritical, then there is no reason why the overall geometry should agree with critical wedge theory. It follows that these types of dynamical models must be constructed as a dynamical system. Merely adding surface processes to a kinematically constructed critical wedge in such a way that the critical taper is maintained (e.g., Dahlen and Suppe, 1988; Dahlen and Barr, 1989, Whipple and Meade, 2004) misses the supercritical branch of the overall system, as well as the feedback of surface processes, in this instance particularly sediment deposition, to the mechanics.

Implications of Model Results for Fault Strength

The very weak and thin detachment layers specified in the models host narrow zones of very high shear strain. These zones appear to emulate fault zones in that they allow the development of features characteristic of TFBs, including structures that emulate far-traveled and little-deformed thrust sheets, duplexes and antiformal stacks. As noted above, numerical models that have significantly less strength contrast

between the thin detachment layers and the thick stronger layers do not develop these types of structures, but rather deform in a quasi-pure shear fashion, with strain more equally distributed across all layers. Very weak detachments (relative to the thick layers) appear essential, in the present model formulation, to produce experiments that look like natural TFBs.

The implication is that natural faults must not merely be weak, but that they must be *extremely* weak, relative to the strength of thrust sheets at the time of deformation. Stronger faults would result in a larger partitioning of shortening within the wedge being accommodated *within* thrust sheets rather than being concentrated on relatively few large fault zones. Note that elevated pore fluid pressures, widely invoked as an explanation for large overthrusts subsequent to the seminal work of Hubbert and Rubey (1951), cannot easily account for this implied strength contrast in natural thrust-and-fold belts, unless there is an extreme difference in pore fluid pressure between the fault zones and the thrust sheets. The production and maintenance of such a pressure difference over extended periods of time, or its episodic production, are problematic.

Price (1988) considered the issue of “The mechanical paradox of large overthrusts”, and suggested that the explanation may lie in the nature of individual local displacement events (e.g., earthquakes). He concluded that large overthrusts are “not (controlled) by the frictional resistance to sliding integrated over the entire fault surface”, because the entire fault surface does not fail simultaneously. However, considered from the point of view of an energy or mechanical work argument, and integrating over *time* as well as space, large overthrusts must have extremely low frictional strength, at least episodically. Our numerical models, which derive from a variational (minimum

dissipation or minimum work) formulation, support this view. Furthermore, recent laboratory studies of sliding friction at displacement rates approaching those of seismic events indicate a profound lowering of frictional resistance (e.g., Di Toro et al., 2004, where resistance extrapolates to zero at seismic slip rates of ~1 m/s) in which water may play a role, but not necessarily in the form of high pore fluid pressure. Our numerical models suggest that the reality of extremely low fault strength (by whatever mechanism) is recorded by the geometry of thin-skinned thrust-and-fold belts.

Implications for Kinematic Models

Kinematic models for structures within thin-skinned TFBs will continue to play an important role in academic as well as industry studies. However, the development of dynamical models, such as those presented here, can greatly improve the awareness and “intuition” of a researcher or explorationist constructing a kinematic model, by demonstrating some of the complexities that can arise in fully coupled systems. For example, kinematic models are commonly constructed assuming an in-sequence structural development, with most if not all of the motion on a particular fault complete prior to motion on the next in-sequence feature. Perhaps by being more aware of alternatives illuminated by dynamical models, researchers and explorationists may find evidence of important structures overlooked in areas of less-than-optimal subsurface data.

Model Limitations and Future Work

The principal limitations of our current numerical models include: (1) fault zones are represented by finite thickness shears, (2) very weak, bedding-parallel detachments are embedded in initial model configurations to emulate fault zones, (3) surface process

models are extremely simple, (4) thermal evolution and wedge thickening through the brittle-ductile transition are not incorporated, and (5) the initial, undeformed model geometry does not have a wedge shape, unlike most natural systems (fundamental characteristic 3, of Chapple (1978), noted above).

Limitation (1) is a consequence of the continuum modelling approach adopted. The creeping, viscous-plastic, Stokes flow, FE formulation of Fullsack (1995) and Beaumont et al. (2004) does not accommodate discrete, one-dimensional surfaces. However, the Eulerian FE grid is sufficiently fine that the high shear strain zones that emulate faults are very narrow (a few elements wide) in comparison to the entire model thickness. Higher resolution models can improve this situation, but there are practical computer computational limits.

Limitation (2) is a compromise as this stage of our investigations, but it does parallel approaches often taken in analogue models where thin, weak materials are embedded to promote faulting (e.g., Leturmy et al., 2000). Future efforts will involve materials that are initially strong but adopt fault-like (extremely weak) strain- and strain-rate dependent properties, possibly coupled to dynamical pore pressure evolution.

Limitation (3) reflects our intention here to use only the simplest formulations for erosion and sedimentation. These simplifications are justified at this stage, but future work will examine the sensitivity of the structural style to more complex erosional and depositional models, such as allowing multiple base levels, resulting in perched piggy-back basins, and due consideration of the plan-form nature of surface processes.

Limitation (4) will be eliminated in future work. We anticipate that it may help to reduce some of the boundary condition effects related to the rigid backstop. See Williams et al. (1994) for an analysis applicable to whole-wedge critical wedges.

Limitation (5) will also be eliminated in future work. Our intention here was to make the fewest number of assumptions, and deal with the fewest number of variables, in order to produce models that effectively emulated natural TFBs.

Conclusions

Dynamical numerical FE models of thrust-and-fold belts were investigated to gain insight into their predictions concerning structural styles. Examples presented illustrate the influences of accretion of a finite thickness layer, regional flexural isostasy, internal layering and strength contrast, strain-softening, and syndeformational erosion and sedimentation.

The following conclusions are drawn from the models presented here.

(1) We regard the dynamical FE approach to TFB dynamics as a method that promises improved insight into the structural style of natural TFBs at scales below that of the whole wedge.

(2) The set of model results presented provides basic insight into the partitioning of strain within TFB's.

(3) For the most simple models (Figures 3 and 4), comprising a thick strong frictional overburden overlying a thin very weak basal detachment, the fundamental deformation units (the building blocks of the wedge) are pop-up structures, or plugs, that scale according to the thickness of the strong layer at the accretionary front. The

partitioning of strain into non-deforming triangular plugs bounded by shear zones occurs even if the properties of the wedge do not change during deformation. The development of these strain characteristics (plastic slip lines) is most likely a consequence of the boundary conditions, particularly the kinematically imposed velocity singularity at the base of the rear of the wedge. By implication, similar structures seen in analogue sandbox experiments would develop even if the sand did not strain harden or soften. The most simple models also show a tendency to assemble the plugs into larger structural units that resemble short thrust sheets as the deforming wedge thickens (Figure 3).

(4) Equivalent simple models with elastic flexural isostatic compensation (Figure 4) have similar plug characteristics and greater tendency to create thrust sheets, most likely because isostatically compensated wedges are thicker and more shortening is required to achieve critical wedge conditions.

(5) Even these simple wedges show significant sub-wedge scale departures from a uniform taper predicted by critical wedge theory (Figure 4).

(6) Models comprising two equal, thick strong layers, each with a thin very weak underlying detachment, demonstrate that wedges of this type develop thrust sheets in both the upper and lower layers with a tendency for longer thrust sheets in the lower layer (Figure 5). These lower layer thrust sheets become even longer and have less internal deformation when the thick strong layers strain soften (Figure 6).

(7) Significant syn-deformational slope-dependent erosion of the surface of the same two-layer model with strain softening modifies details of the structures, enhances the development of pop-ups in the upper layer, but does not change the overall character

of the deformation (Figure 7). However, the wedge is profoundly modified by the combined effects of slope-dependent erosion and rapid filling of the flexural foreland basin with sediment (Figure 8). This model develops piggy back basins by sequentially detaching significant parts of the undeformed foreland basin because critical wedge conditions are achieved without the need to thicken the strata.

(8) Models with three thick, strong strain-softening layers, separated by very weak detachments, develop structures that most resemble our reference natural example, the Southern Canadian Rocky Mountains (SCRM). In particular, models with slope-dependent erosion and rapidly filled basins develop multiple piggyback basins (Figure 10) which, when eroded, strongly resemble synclines developed in the Foothills of the SCRM (Figure 12).

(9) The overall results demonstrate the importance of treating thin-skinned TFBs as dynamical coupled systems, where continuous feedback among system components shapes the details of internal structure and surface expression.

There are an infinite number of combinations of model parameters, and here we have examined only a few. The degree to which model results are sensitive to these parameters is the subject of on-going investigation. We know that surface processes can play a major role in influencing structural style, but the bounds on those influences are presently uncertain. Unpublished models suggest that over a realistic range of erosion rates (linearly slop-dependent), the overall structural style is not strongly affected, although the details of any particular model can be highly path-dependent. Other unpublished models suggest that syndeformational sedimentation is generally a much stronger influence than erosion, but of course we recognize that in an orogen-

scale scale system (larger than the length-scale of models considered here), the volumes of rock eroded and sediment deposited are intimately related.

Acknowledgements

We wish to thank Ray Price for many years of inspiration and motivation imparted through his Rocky Mountain maps, articles, lectures, and field trips, and through numerous thoughtful and encouraging discussions. We thank _____ and _____ for formal reviews, and Kirk Osadetz and Margot McMechan for internal GSC reviews. This is GSC Contribution #_____.

Appendix

For a plane-strain, two-dimensional case, where σ_1 and σ_3 are the maximum and minimum values of the principal stresses, the mean stress (or solid pressure), P, is:

(A1) $$P = \frac{\sigma_1 + \sigma_3}{2}.$$

In a Mohr-Coulomb material, parameterized by a cohesion value, C_0, and an angle of internal friction, φ, failure may occur if the effective mean stress is reduced due to an increase in pore fluid pressure. At failure, the magnitude of the pore fluid pressure, P_f, is:

(A2) $$P_f = \frac{\sigma_1 + \sigma_3}{2} - \frac{\sigma_1 - \sigma_3}{2\sin\varphi} + \frac{C_0}{\tan\varphi}.$$

In our models, we define the pore fluid pressure ratio relative to the solid pressure:

(A3) $$\lambda = \frac{P_f}{P}.$$

The common Hubbert-Rubey pore pressure ratio is generally defined as:

(A4) $$\lambda_{HR} = \frac{P_f}{P_{overburden}},$$

where $P_{overburden}$ is the weight of the overburden, equal to $\rho g d$, where ρ, g, and d are the mean density, gravitational acceleration, and depth, respectively. The ratio of λ to λ_{HR} is then:

(A5) $$\frac{\lambda}{\lambda_{HR}} = \frac{P_{overburden}}{P}.$$

The minimum principal stress, σ_3, can be approximated as equal to the overburden weight:

(A6) $\sigma_3 \approx \rho g d = P_{overburden}$.

An expression for the maximum principal stress, σ_1, is derived by first substituting (A1) and (A2) into (A3):

(A7) $$\lambda\left(\frac{\sigma_1+\sigma_3}{2}\right)=\frac{\sigma_1+\sigma_3}{2}-\frac{\sigma_1-\sigma_3}{2\sin\varphi}+\frac{C_0}{\tan\varphi},$$

and then solving for σ_1:

(A8) $$\sigma_1=\frac{\sigma_3(1-\lambda+\csc\varphi)+2C_0\cot\varphi}{-1+\lambda+\csc\varphi}.$$

Using A6 and A8 in A5, we find:

(A9) $$\frac{\lambda}{\lambda_{HR}}=\frac{\rho g d(-1+\lambda+\csc\varphi)}{\rho g d\csc\varphi+C_0\cot\varphi}.$$

Using (A9), the Hubbert-Rubey pore pressure ratio, λ_{HR}, can be expressed in terms of our expression of the ratio, λ, as:

(A10) $$\lambda_{HR}=\lambda\left(\frac{\rho g d+C_0\cos\varphi}{\rho g d(1-(1-\lambda)\sin\varphi)}\right).$$

Equation (A10) can be solved iteratively for λ given a value for λ_{HR}.

Note that when the cohesion is either zero or of negligible magnitude, (A9) and (A10) are independent of depth. Although the magnitude of λ_{HR} corresponding to saturated (i.e., hydrostatic) conditions is easily determined (ratio of water and rock densities), under overpressured conditions the correspondence between pore fluid pressure and solid pressure, as in (A3), is more intuitive.

For a hydrostatically pressured case, where the average density of the thrust-and-fold belt is 2300 km/m^3, the value of λ_{HR} is 1000/2300, or 0.435. When the cohesion is negligible or zero, the corresponding value of λ is 0.278, assuming φ is 30°. In our

formulation of effective angle of internal friction (equation (2), main text), a dry value of 30° would reduce to 21° under these conditions.

References

Beaumont, C., 1981. Foreland basins. Geophysical Journal of the Royal Astronomical Society, v. 65, p. 291-329.

Beaumont, C., Fullsack, P., and Hamilton, J., 1992. Erosional control of active compressional orogens. In: *Thrust Tectonics*, K.R. McClay (ed.), Chapman and Hall, New York, p. 1-18.

Beaumont, C., Jamieson, R.A., Nguyen, M.H., and Medvedev, S., 2004. Crustal channel flows: 1. Numerical models with applications to the tectonics of the Himalayan-Tibetan orogen. Journal of Geophysical Research, v. 109, B06406 (29 p.).

Beaumont, C., Kooi, H., and Willett, S., 2000. Coupled tectonic-surface process models with applications to rifted margins and collisional orogens. In: Geomorphology and Global Tectonics, M.A. Summerfield (ed.), John Wiley & Sons, p. 29-55.

Bos, B., and Spiers,C.J., 2002, Frictional-viscous flow of phyllosilicate-bearing fault rock: microphysical model and implications for crustal strength profiles. Journal of Geophysical Research, v.107, p.doi:10,10129/2001JB000301.

Braun, J., and Sambridge, M., 1997. Modelling landscape evolution on geological time scales: a new method based on irregular spatial discretization. Basin Research, v. 9, p. 27-52.

Byerlee, J., 1978. Friction of rocks. Pure and Applied Geophysics, v. 116, p. 615-626.

Chapple, W.M., 1978. Mechanics of thin-skinned fold-and-thrust belts. Geological Society of America Bulletin, v. 89, p. 1189-1198.

Chery, J., Zoback, M.D., and Hassini, R., 2001, An integrated mechanical model of the San Andreas fault in central and northern California. Journal of Geophysical Research, v.106, p. 22,051-22,066.

Connolly, J.A.D., and Podladchikov, Y.Y., 2000, Temperature-dependent viscoelastic compaction and compartmentalization in sedimentary basins, Tectonophysics, v. 324.p. 137-168.

Cooke, M.L., and Murphy, S., 2004. Assessing the work budget and efficiency of fault systems using mechanical models. Journal of Geophysical Research, v. 109, B10408, 13 p.

Davis, D., Suppe, J., and Dahlen, F.A., 1983. Mechanics of fold-and-thrust belts and accretionary wedges. Journal of Geophysical Research, v. 88, p. 1153-1172.

Dahlen, F.A., 1984. Noncohesive critical Coulomb wedges: an exact solution. Journal of Geophysical Research, v. 89, p. 10,125-10,133.

Dahlen, F.A., 1988. Mechanical energy budget of a fold-and-thrust belt. Nature, v. 331, p. 335-337.

Dahlen, F.A., 1990. Critical taper model of fold-and-thrust belts and accretionary wedges. Annual Reviews of Earth and Planetary Sciences, v. 18, p. 55-99.

Dahlen, F.A., and Barr, T.D., 1989. Brittle frictional mountain building 1. Deformation and mechanical energy budget. Journal of Geophysical Research, v. 94, p. 3906-3922.

Dahlen, F.A., and Suppe, J., 1988. Mechanics, growth, and erosion of mountain belts. Geological Society of America, Special Paper 218, p. 161-178.

Dahlen, F.A., Suppe, J., and Davis, D., 1984. Mechanics of fold-and-thrust belts and accretionary wedges: cohesive Coulomb theory. Journal of Geophysical Research, v. 89, p. 10,087-10,101.

Di Toro, G., Goldsby, D.L., and Tullis, T.E., 2004. Friction falls towards zero in quartz rock as slip velocity approaches seismic rates. Nature, v. 427, p. 436-439.

Fullsack, P., 1995. An arbitrary Lagrangian-Eulerian formulation for creeping flows and its application in tectonic models. Geophysical Journal International, v. 120, p. 1-23.

Hacquebard, P.A. 1977. Chapter 3 – Rank of coal as an index of organic metamorphism for oil and gas in Alberta. In: *The Origin and Migration of Petroleum in the Western Canadian Sedimentary Basin*, G. Deroo, T.G. Powell, B. Tissot, and R.G. McCrossan (eds.). Geological Survey of Canada, Bulletin 262, p. 11-22.

Hardy, S., Duncan, C., Masek, J., and Brown, D., 1998. Minimum work, fault activity and the growth of critical wedges in fold and thrust belts. Basin Research, v. 10, p. 365-373.

Hill, R., 1950. The Mathematical Theory of Plasticity. Oxford University Press, 355 p.

Hubbert, M.K., 1951. Mechanical basis for certain familiar geologic structures. Geological Society of America Bulletin, v. 62, 355-372.

Hubbert, M.K., and Rubey, W.W., 1959. Role of fluid pressure in mechanics of overthrust faulting. Geological Society of America Bulletin, v. 70, p. 115-166.

Ingebritsen, S.E., and Manning, C.E., 1999, Geological implications of a permeability-depth curve for the continental crust, Geology, v. 27, p. 1107-1110.

Leturmy, P., Mugnier, J.L., Vinour, P., Baby, P., Colletta, B., and Chabron, E., 2000. Piggyback basin development above a thin-skinned thrust belt with two detachment levels as a function of interactions between tectonic and superficial mass transfer: the case of the Subandean Zone (Bolivia). Tectonophysics, v. 320, p. 45-67.

Liu, H., McClay, K.R., and Powell, D., 1992. Physical models of thrust wedges. In: *Thrust Tectonics*, K.R. McClay (ed.), Chapman and Hall, New York, p. 71-81.

Masek, J.G., and Duncan, C.C., 1998. Minimum work mountain building. Journal of Geophysical Research, v. 103, p. 907-917.

Mitra, G., and Boyer, S.E., 1986. Energy balance and deformation mechanisms of duplexes. Journal of Structural Geology, v. 8, p. 291-304.

Mountjoy, E.W., Windh, J., Price, R.A., and Douglas, R.J.W., 2002. Geology, George Creek, Alberta. Geological Survey of Canada, Map 1990A, 1:50,000, 2 sheets.

Nurkowski, J.R., 1984. Coal quality, coal rank variation and its relation to reconstructed overburden, Upper Cretaceous and Tertiary Plains coals, Alberta. American Association of Petroleum Geologists Bulletin, v. 68, p. 285-295.

Ollerenshaw, N.C., 1978. Geology, Calgary, Alberta-British Columbia. Geological Survey of Canada, Map 1457A, scale 1:250,000 (2 sheets).

Ori, G.G., and Friend, P.F., 1984. Sedimentary basins formed and carried piggyback on active thrust sheets. Geology, v. 12, p. 475-478.

Osborn, G., Stockmal, G., and Haspel, R., in press. Emergence of the Canadian Rockies and adjacent plains: a comparison of physiography between end-of-Laramide time and the present day. Geomorphology.

Patterson, M.S., 1978. Experimental Rock Deformation – The Brittle Field. Springer-Verlag, New York, 254 p.

Pivnik, D.A., and Khan, M.J., 1996. Transition from foreland- to piggyback-basin deposition, Plio-Pleistocene Upper Siwalik Group, Shinghar Range, NW Pakistan. Sedimentology, v. 43, p. 631-646.

Pieri, M., 1989. Three seismic profiles through the Po Plain. In: *Atlas of Seismic Stratigraphy, Volume 3*, A.W. Bally (ed.), AAPG Studies in Geology #27, p. 90-110.

Price, R.A., 1973. Large-scale gravitational flow of supracrustal rocks, southern Canadian Rockies. In: *Gravity and Tectonics*, K.A. de Jong, and R. Scholten (eds.), Wiley, New York, p. 491-502.

Price, R.A., 1981. The Cordilleran foreland thrust and fold belt in the southern Canadian Rocky Mountains. In: *Thrust and Nappe Tectonics*, K.R. McClay, and N.J. Price (eds.), Geological Society of London Special Publication No. 9, p. 427-448.

Price, R.A., 1988. The mechanical paradox of large overthrusts. Geological Society of America Bulletin, v. 100, p. 1898-1908.

Price, R.A., 2001. An evaluation of models for the kinematic evolution of thrust and fold belts: structural analysis of a transverse fault zone in the Front Ranges of the Canadian Rockies north of Banff, Alberta. Journal of Structural Geology, v. 23, pp. 1079-1088.

Price, R.A., and Fermor, P.R., 1985. Structure section of the Cordilleran foreland thrust and fold belt west of Calgary, Alberta. Geological Survey of Canada, Paper 84-14, 1 sheet.

Provost, A.-S., and Houston, H., 2003, Stress orientations in Northern and Central California; evidence for the evolution of frictional strength along the San Andreas plate boundary system, Journal of Geophysical Research., v. 108, p. 18.

Ramos, E., Busquets, P., and Vergés, J., 2002. Interplay between longitudinal fluvial and transverse alluvial fan systems and growing thrusts in a piggyback basin (SE Pyrenees). Sedimentary Geology, v. 146, p. 105-131.

Ramos, V.A., Zapata, T., Cristallini, E., and Introcaso, A., 2004. The Andean thrust system – Latitudinal variations in structural style and orogenic shortening. In: *Thrust Tectonics and Hydrocarbon Systems*, K.R. McClay (ed.), AAPG Memoir 82, p. 30-50.

Rice, J.R., 1992, Fault stress states, pore pressure distributions, and the weakness of the San Andreas Fault, B. Evans, and T.F.Wong, (eds), *Fault Mechanics and Transport Properties of Rocks*: London, Academic Press, p. 475-503.

Ridley, J., 1993, The relations between mean rock stress and fluid flow in the crust: with reference to vein- and lode-style gold deposits: Ore Geol. Rev., v. 8, p. 23-37.

Roe, G.H., Montgomery, D.R., and Hallet, B., 2003. Orographic precipitation and the relief of mountain ranges. Journal of Geophysical Research, v. 108, B6, 2315 (11 p.).

Scholz, C.H., 1990, *The Mechanics of Earthquakes and Faulting,* Cambridge, Cambridge University Press, 439 p.

Schultz, R.A., 1996. Relative scale and the strength and deformability of rock masses. Journal of Structural Geology, v. 18, p. 1139-1149.

Sibson, R.H., 1990, Conditions for fault-valve behaviour, R.J. Knipe, and E.H. Rutter, (eds), *Deformation Mechanisms, Rheology and Tectonics*, v. 54, London, Geological Society Special Publications, p. 15-28.

Stockmal, G.S., 1983. Modeling of large-scale accretionary wedge deformation. Journal of Geophysical Research, v. 88, p. 8271-8287.

Stockmal, G.S., Lebel, D., McMechan, M.E., and MacKay, P.A., 2001. Structural style and evolution of the triangle zone and external Foothills, southwestern Alberta: Implications for thin-skinned thrust-and-fold belt mechanics. Bulletin of Canadian Petroleum Geology, v. 49, p. 472-496.

Streit, J.E., 1997, Low frictional strength of upper crustal faults; a model, Journal of Geophysical Research, v. 102, p. 24,619-24,626.

Whipple, K.X., and Meade, B.J., 2004. Controls on the strength of coupling among climate, erosion, and deformation in two-sided, frictional orogenic wedges at steady state. Journal of Geophysical Research, v. 109, F01011 (24 p.).

Willett, S.D., 1999. Orogeny and orography: The effects of erosion on the structure of mountain belts. Journal of Geophysical Research, v. 104, p. 28, 957-28,981.

Willett, S.D., Slingerland, R., and Hovius, N., 2001. Uplift, shortening, and steady state topography in active mountain belts. American Journal of Science, v. 301, p. 455-485.

Williams, C.A., Connors, C., Dahlen, F.A., Price, E.J., and Suppe, J., 1994. Effect of the brittle-ductile transition on the topography of compressive mountain belts on Earth and Venus. Journal of Geophysical Research, v. 99, p. 19,947-19,974.

Materials	φ_{eff} (°)	C_0 (Mpa)	ε-range	ρ (kg/m^3)
Strong, no strain-softening	38	2	n/a	2300
Strong, with strain-softening	38→18	2	0.5→1.0	2300
Very weak, basal detachment layer	3.5	2	n/a	2300
Very weak, internal detachment layer	1	2	n/a	2300
Sediment	38→18	2	0.5→1.0	2300

Material Strength Comparisons

φ_{eff} (°)	$\sin(\varphi_{eff})$	$\sin(\varphi_{eff})/\sin(38°)$	$\tan(\varphi_{eff})$	λ	λ_{HR}*
38	0.616	1.0	0.781	0	0
18	0.309	0.50	0.325	0.50	0.72
3.5	0.0610	0.10	0.0617	0.90	0.96
1	0.0175	0.028	0.0175	0.97	0.99

Initial Configuration	*Horizontal*		*Vertical*	
	Cells (#)	*Dimension (km)*	*Cells (#)*	*Dimension (km)*
Eulerian Mesh	800	200	78	5
Lagrangian Mesh	3200	800	78	5

Boundary Conditions

Left side	Above 256.41 m from base: zero horizontal velocity, zero shear stress Below 256.41 m from base: material exits to left at rate of 10 mm/yr
Right side	Lagrangian mesh enters from right at rate of 10 mm/yr
Bottom	Bottoms of basal elements move to left at rate of 10 mm/yr
Top	Stress free; subject to erosion and/or sedimentation

Flexure Options

- Rigid base
- Elastic base – either constant or variable flexural rigidity

Surface Processes

Erosion - Linearly dependent on surface slope

- 1 mm/yr on 1:1 slope

Sedimentation – Dependent upon base level specification

- No sedimentation, except minor infilling of tight folds, related to surface definition during Eulerian re-gridding
- Filling of all accommodation space up to base level

Table 1: Properties, parameters, and options common to all numerical models.

* The Hubbert-Rubey pore pressure ratio assumes the cohesion is negligible.

Model #	Number of detachments	Strain-softening strong layers	Flexural base	Surface processes
1	1	No	No	No erosion or sedimentation
2	1	No	***Yes 10^{23} Nm***	No erosion or sedimentation
3	***2***	No	Yes 10^{23} Nm	No erosion or sedimentation
4	2	***Yes***	Yes 10^{23} Nm	No erosion or sedimentation
5	2	Yes	Yes 10^{23} Nm	***Erosion only***
6	2	Yes	Yes 10^{23} Nm	Erosion ***and sedimentation*** (to base level)
7	***3***	Yes	Yes 10^{23} Nm	***No erosion or sedimentation***
8	3	Yes	Yes 10^{23} Nm	***Erosion and sedimentation*** (to base level)

Table 2: Summary of numerical models. The parameters varied from one model to the next are in ***bold italics***.

Figure Captions

Figure 1: Balanced cross-section of the Southern Canadian Rocky Mountains (SCRM), at the latitude of Calgary, Alberta (after Price and Fermor, 1985). The SCRM are considered an archetypal thin-skinned thrust-and-fold belt, and used as a general guide for scaling and interpretation of the numerical models. The positions of two principal detachments are indicated. Post-deformational erosion has removed approximately 2-3 km of foreland basin strata at the deformation front, and correspondingly more of the deformed wedge farther to the west (left).

Figure 2: Model configurations and boundary conditions for the 1-, 2-, and 3-detachment models. Vertical exaggeration = 10 X. See text for discussion.

Figure 3: Model 1 results (1-detachment model with rigid, horizontal base); frames are spaced equally in time. Elapsed time since beginning of convergence and magnitude of convergence are shown. Illustrated width is 200 km, encompassing the entire Eulerian grid. Cells within the Eulerian grid are coloured according to material type (see Figure 2 and Table 1), and the Lagrangian mesh is shown by black lines (only every third mesh line, horizontally and vertically, is drawn for clarity). Dashed line above wedge in (c) is a visual fit to the tops of the pop-up structures, with a slope of 1.6°. Solid lines connecting the topographic low points of the upper surfaces in (a) through (d) have slopes equal to that predicted by the Dahlen (1984) equations for Model 1 materials (0.835°). Arrows in (h) indicate shear zones with relatively large displacements resulting from self-organization of the wedge.

Figure 4: Model 2 results (1-detachment model; addition of flexural isostasy). See Figure 3 caption.

Figure 5: Model 3 results (2-detachment model; addition of an internal detachment layer). See Figure 3 caption.

Figure 6: Model 4 results (2-detachment model; addition of strain-softening within the thick, strong layers). See Figure 3 caption.

Figure 7: Model 5 results (2-detachment model; addition of significant, slope-dependent surface erosion). See Figure 3 caption.

Figure 8: Model 6 results (2-detachment model; addition of sedimentation to specified base level). See Figure 3 caption. OOS – out-of-sequence.

Figure 9: Model 7 results (3-detachment model; erosion only). See Figure 3 caption.

Figure 10: Model 8 results (3-detachment model; erosion and sedimentation). See Figure 3 caption. OOS – out-of-sequence.

Figure 11: Instantaneous velocities and strain-rates for Model 8.

Figure 12: (a) Cross-section across the SCRM Foothills, approximately 100 km NW of Calgary, Alberta (after Ollerenshaw, 1978). (b) Cross-section across the SCRM Foothills, approximately 250 km NW of Calgary, Alberta (after Mountjoy et al., 2002). (c) Cross-section across the Sub-Andean belt, northern Argentina, showing broad synclines occupied by synorogenic sediments documenting out-of-sequence and simultaneous motion on a series of thin-skinned thrusts (after Ramos et al., 2004). In all cases, the relatively undeformed synclines, separated by anticlinal culminations characterized by a concentration of contractional

structures, are similar to those produced in numerical models incorporating syndeformational sedimentation.

Figure 13: Relationships between contractional structures and syndeformational sedimentation seen in (a) the Po Plain (Pieri, 1989), in comparison to portions of Model 8 at (b) 21 My, and (c) 24 My.

Figure 14: Comparison between external wedge geometries (thick grey lines) of three time frames from Model 8 (12, 15, and 18 My), and critical wedge solutions. (a) Linear regression fits to the upper and basal surfaces of the three time frames (long-dashed lines), with slopes of the upper (α) and basal (β) surfaces indicated, along with slopes determined more locally (dotted lines) by fitting minimum topography on the upper surface and very long detachments on the basal surface, with local slope values in parentheses. The local slopes are determined near the wedge-front, and for the 15 and 18 My wedges, also near the wedge-middle. (b) Plots of acceptable combinations of the effective angle of internal friction within the wedge, φ_{eff}, and the effective angle of basal sliding friction, $\varphi_{b,eff}$, for each of the three time frames, and for whole-wedge (WW), wedge-front (W-F) and wedge-middle (W-M) values, using equations of Dahlen (1984).

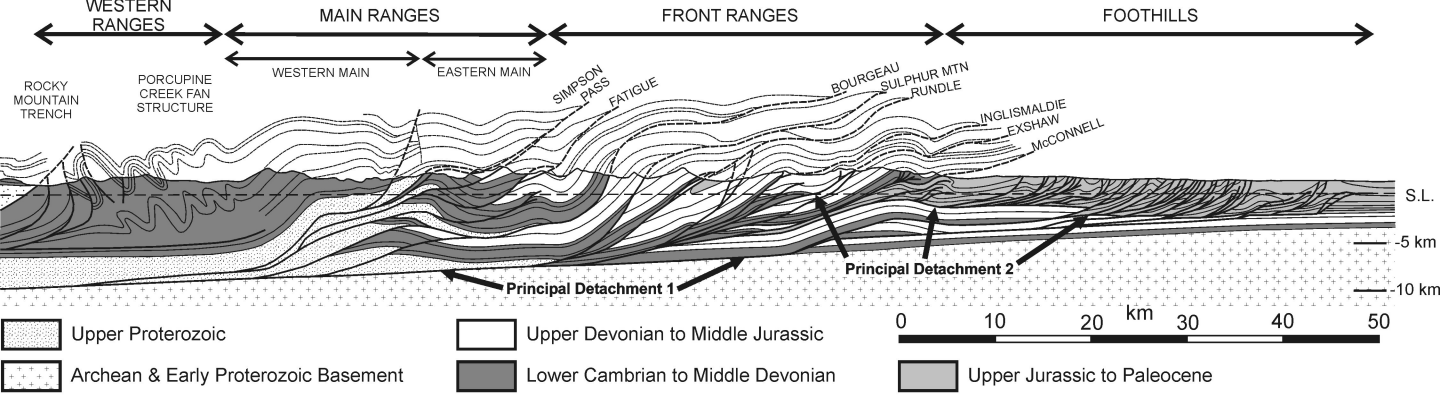

Stockmal et al., Figure 1 (Price vol.)

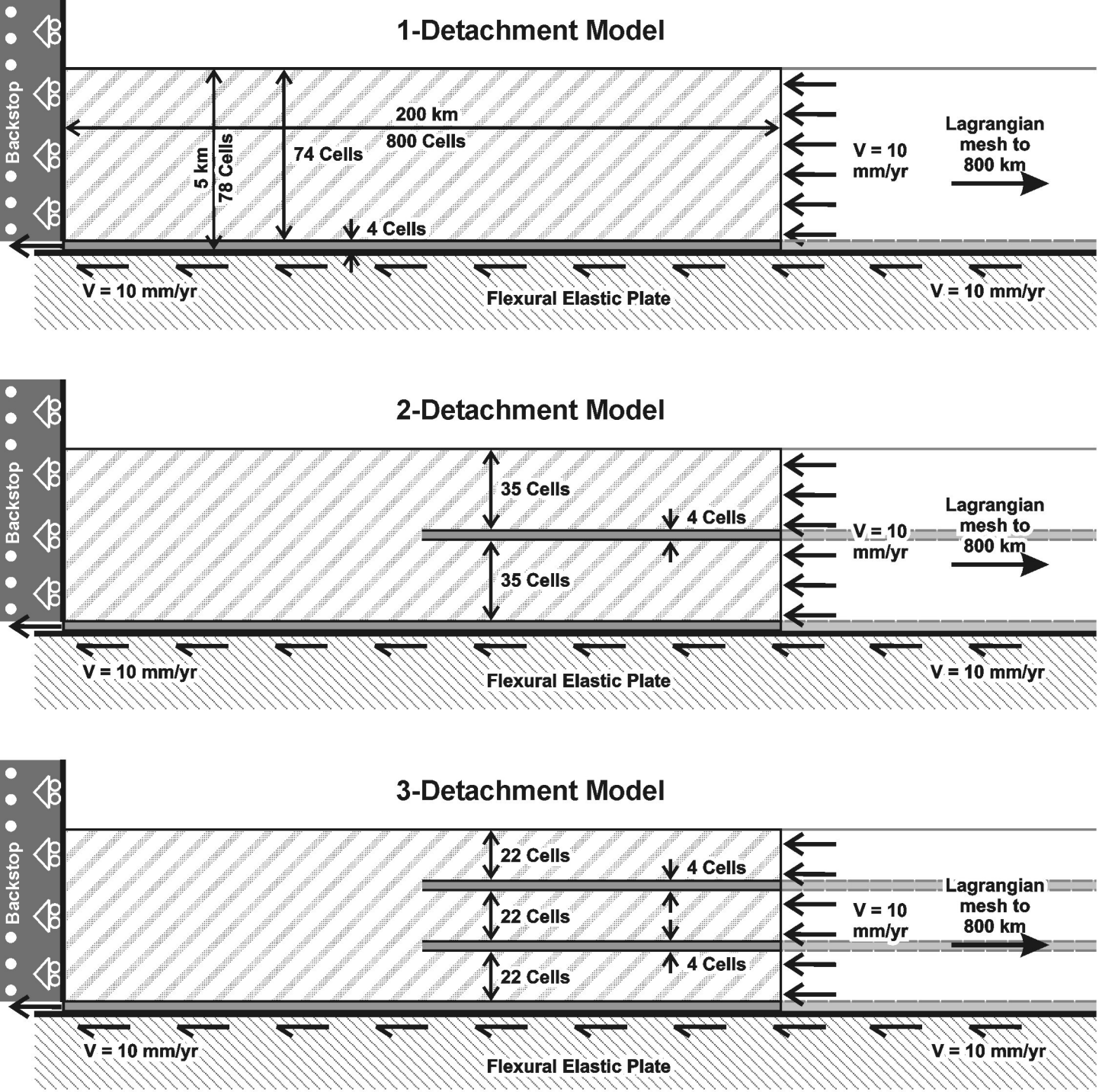

Stockmal et al., Figure 2 (Price vol.)

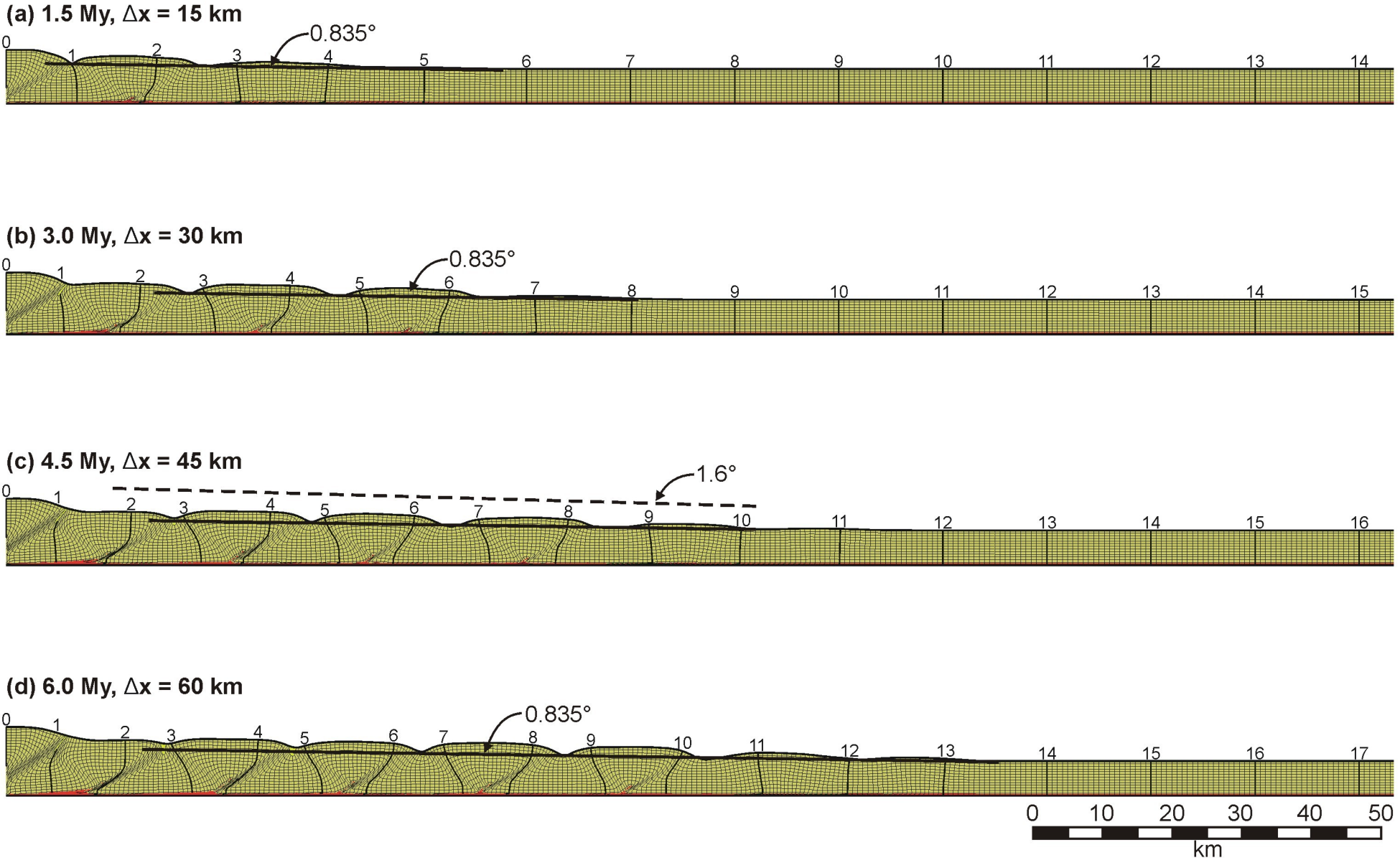

Stockmal et al., Figure 3, part 1 (Price vol).

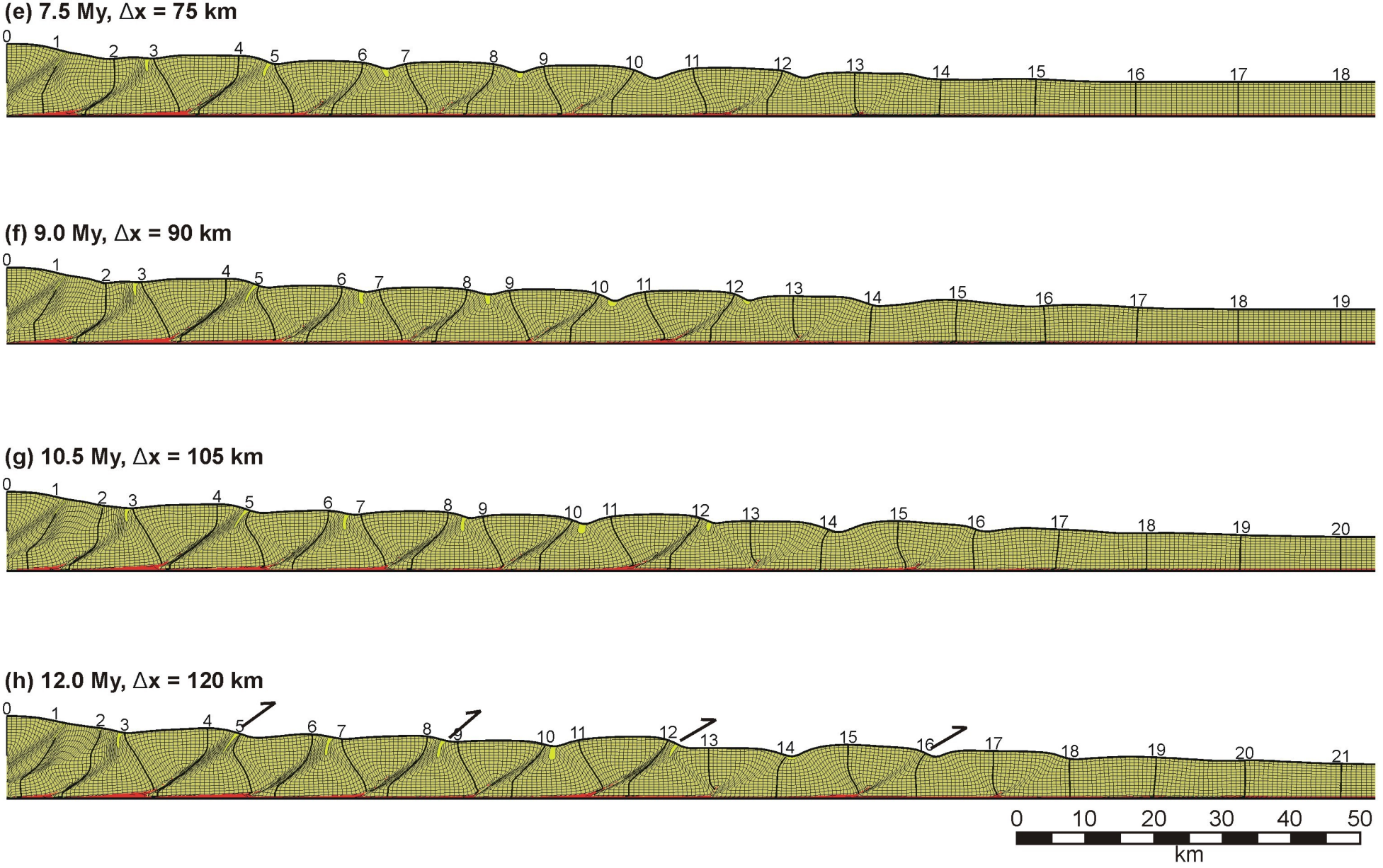

Stockmal et al., Figure 3, part 2 (Price vol).

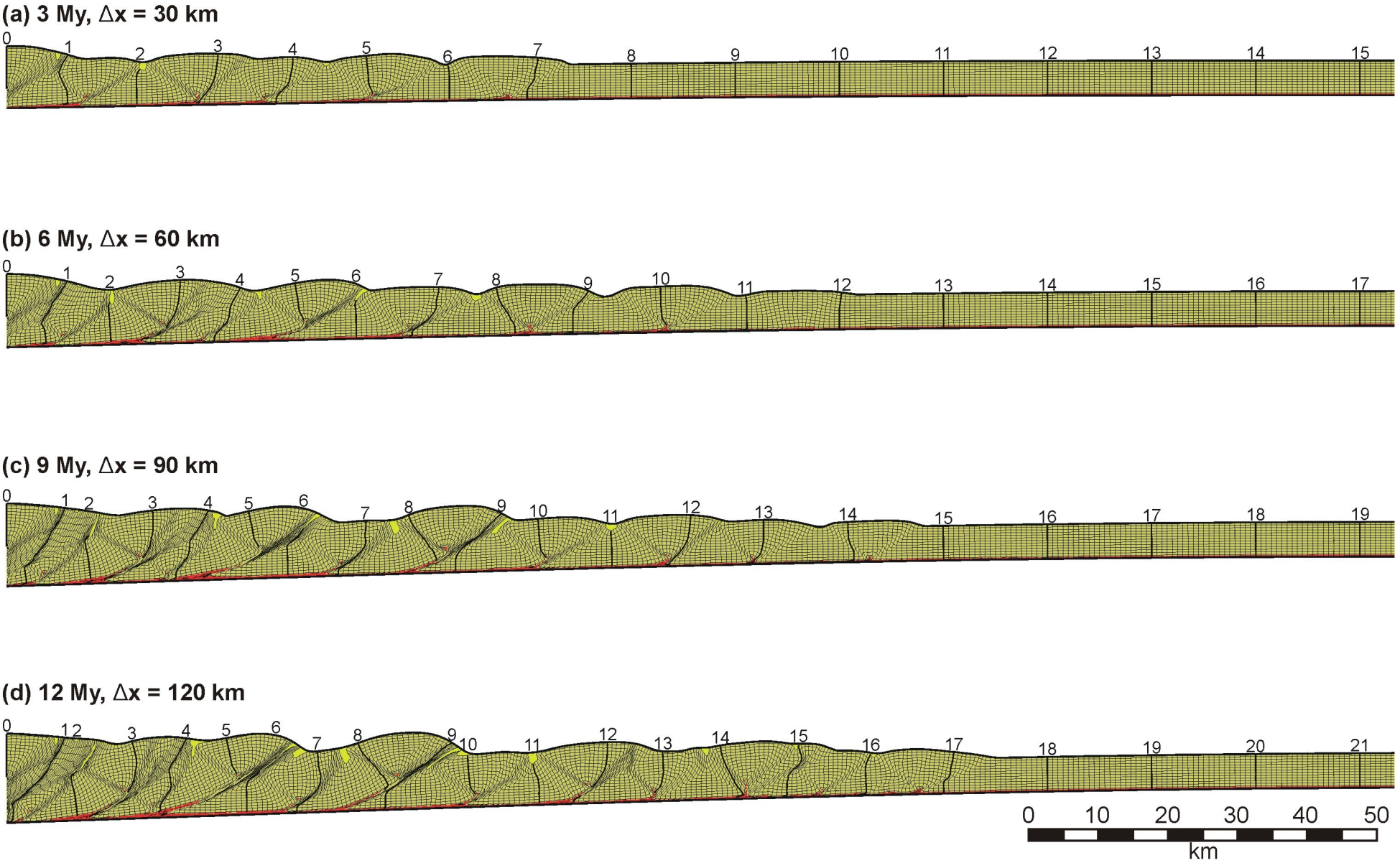

Stockmal et al., Figure 4, part 1 (Price vol).

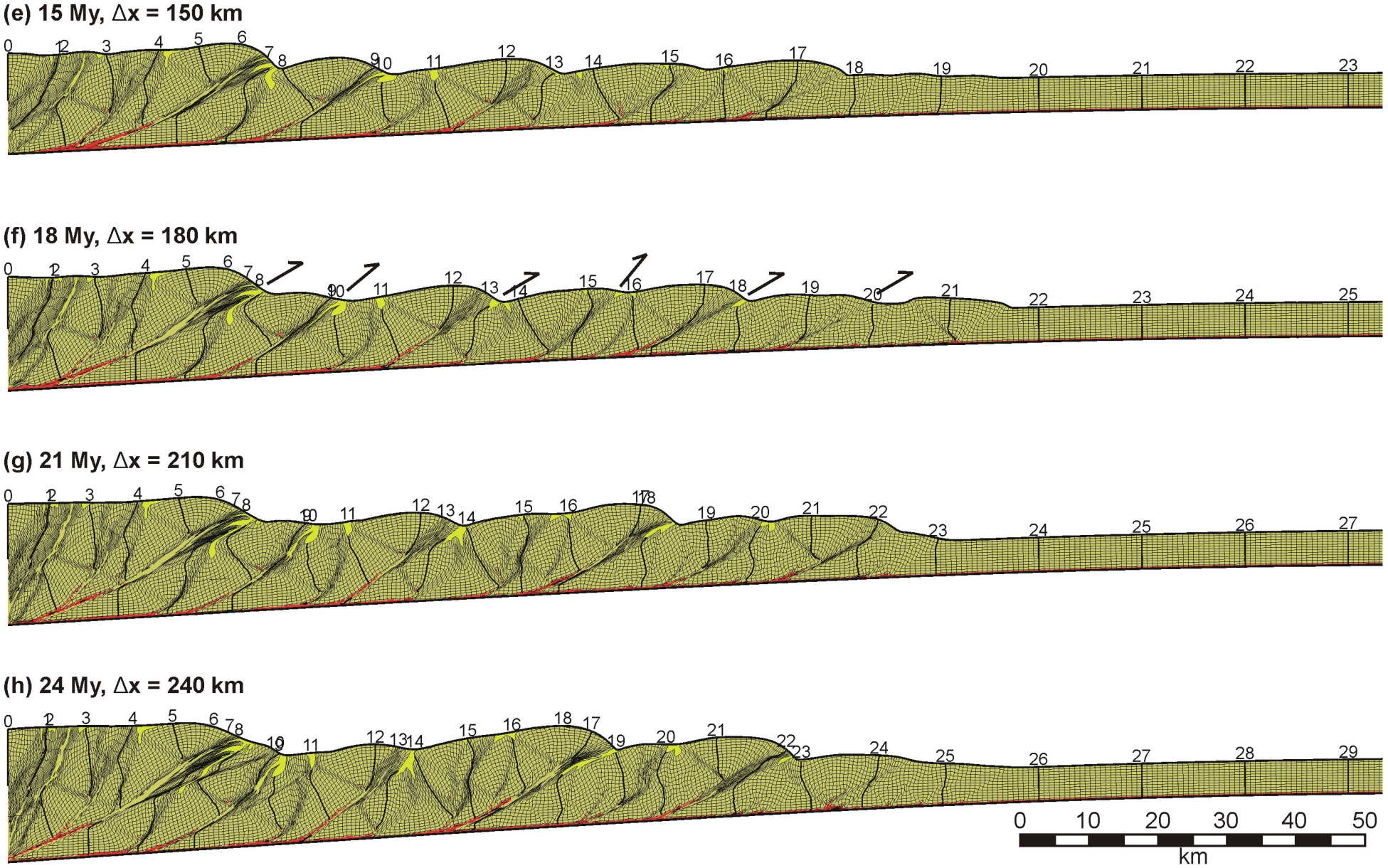

Stockmal et al., Figure 4, part 2 (Price vol).

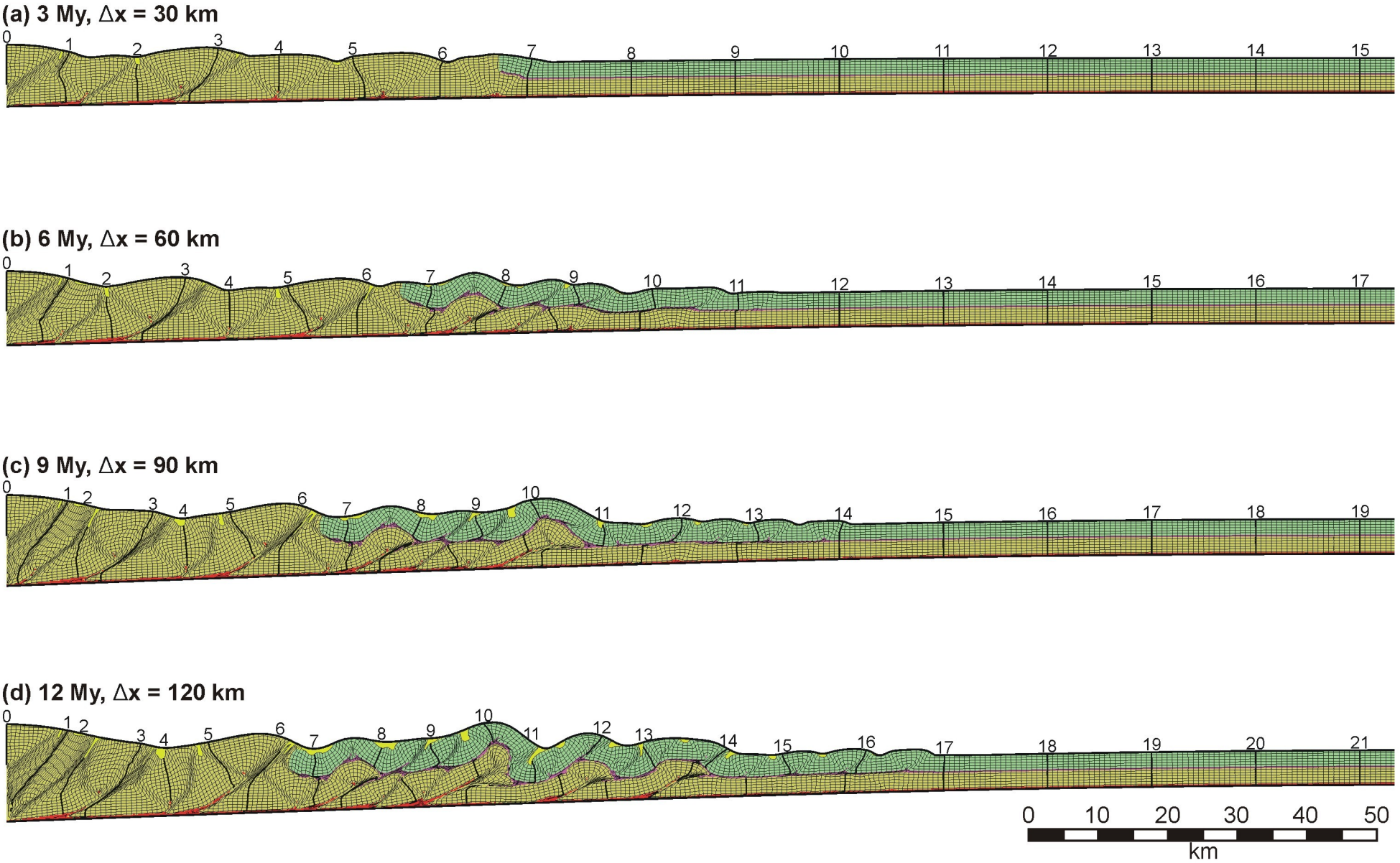

Stockmal et al., Figure 5, part 1 (Price vol).

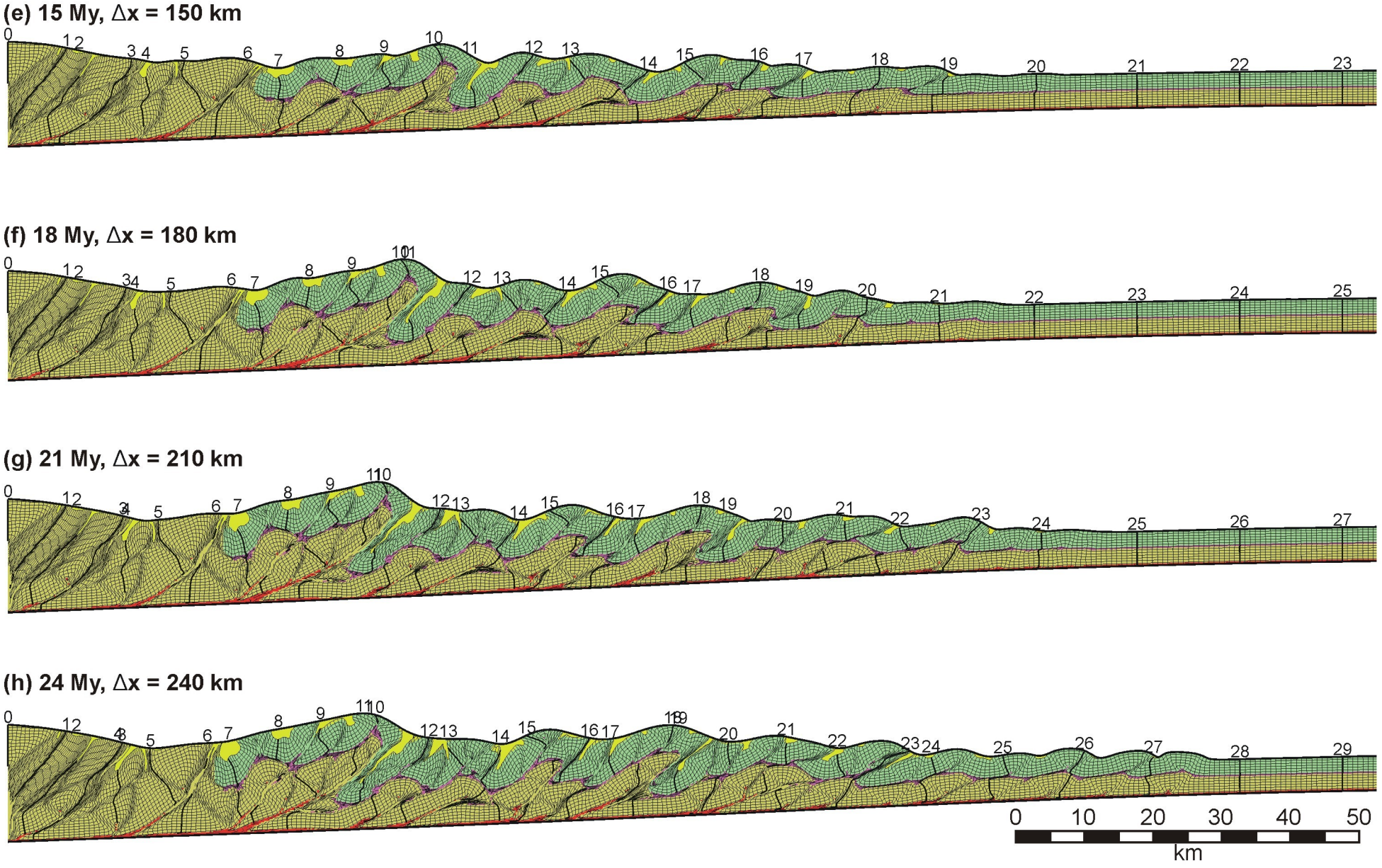

Stockmal et al., Figure 5, part 2 (Price vol).

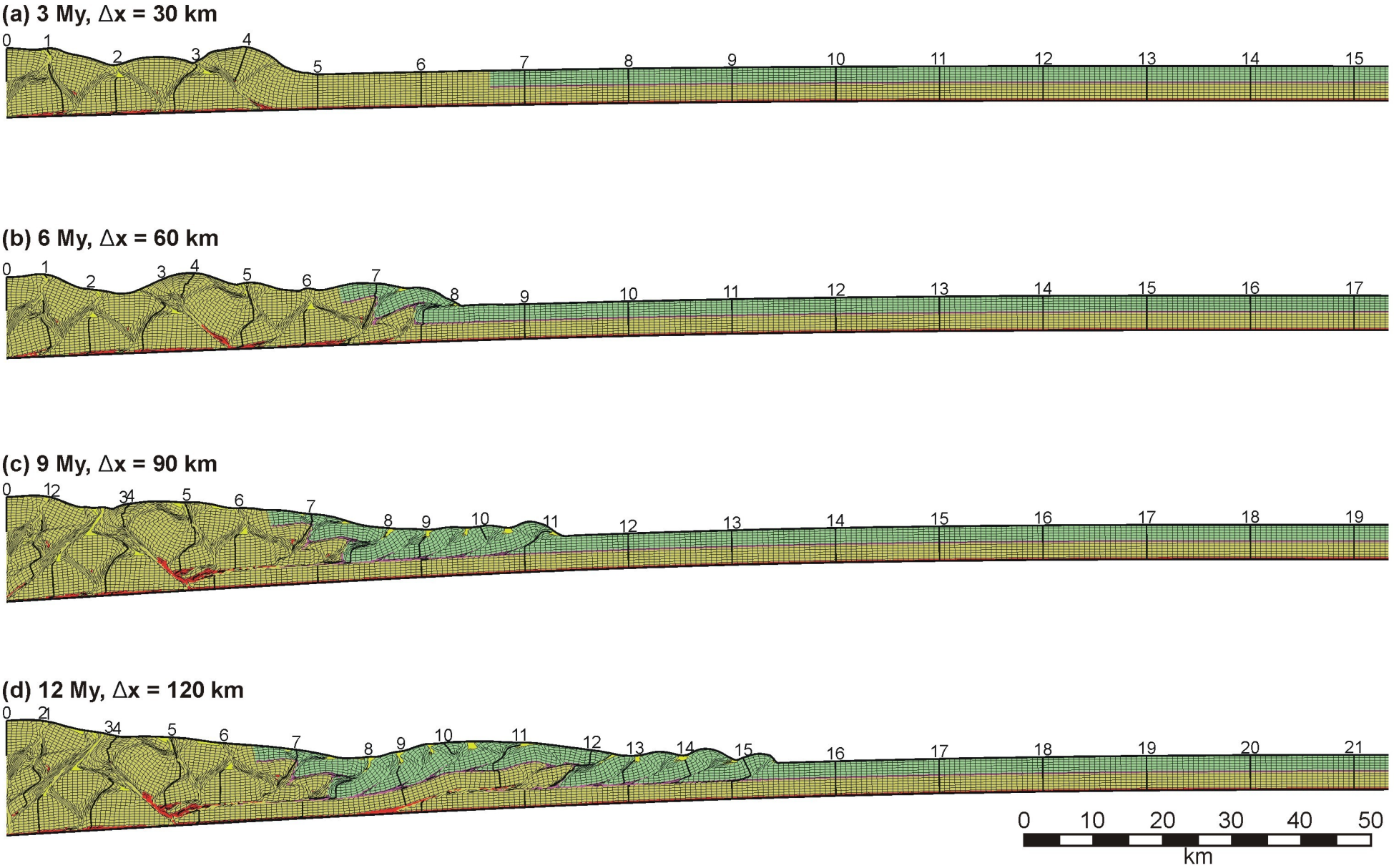

Stockmal et al., Figure 6, part 1 (Price vol).

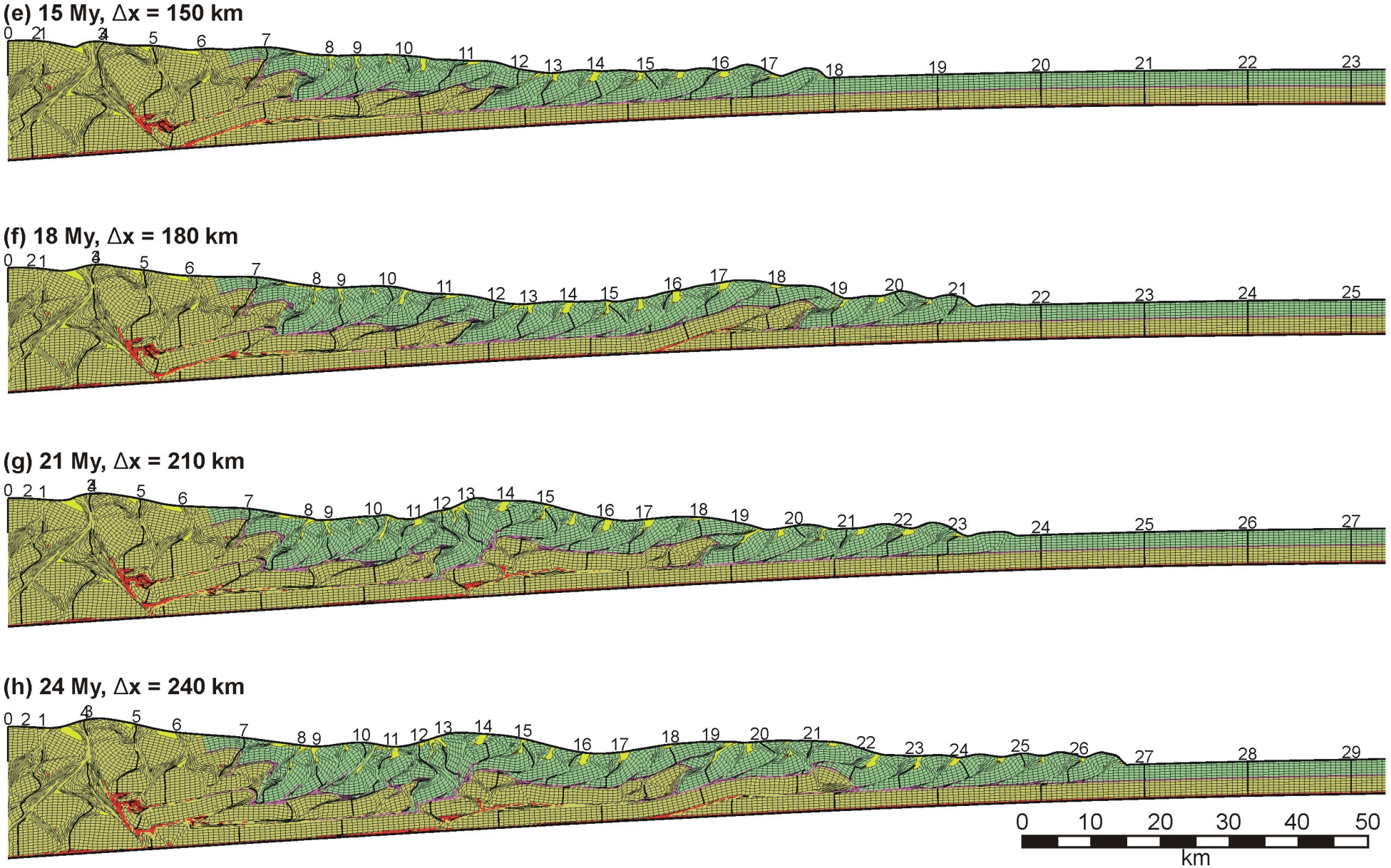

Stockmal et al., Figure 6, part 2 (Price vol).

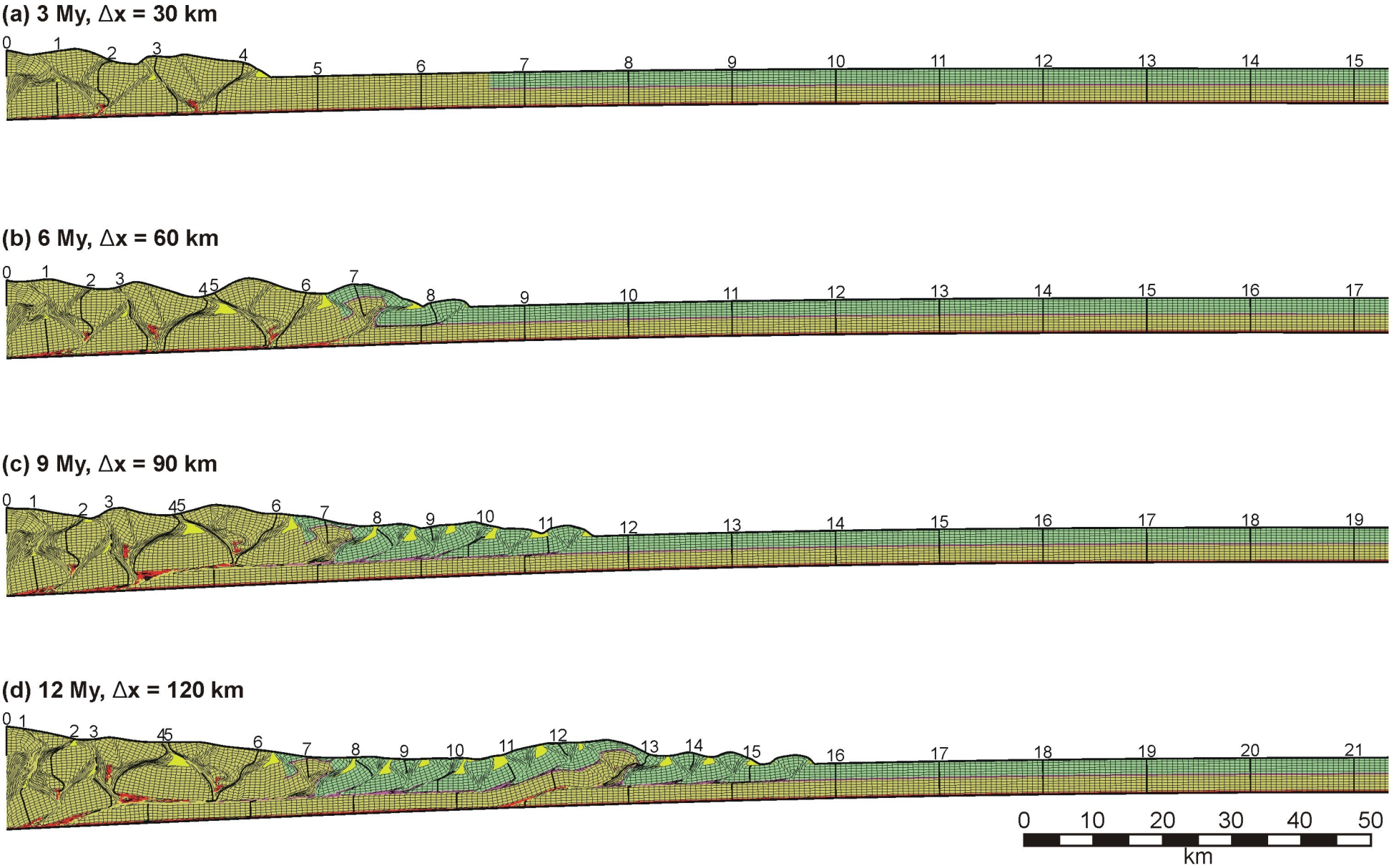

Stockmal et al., Figure 7, part 1 (Price vol).

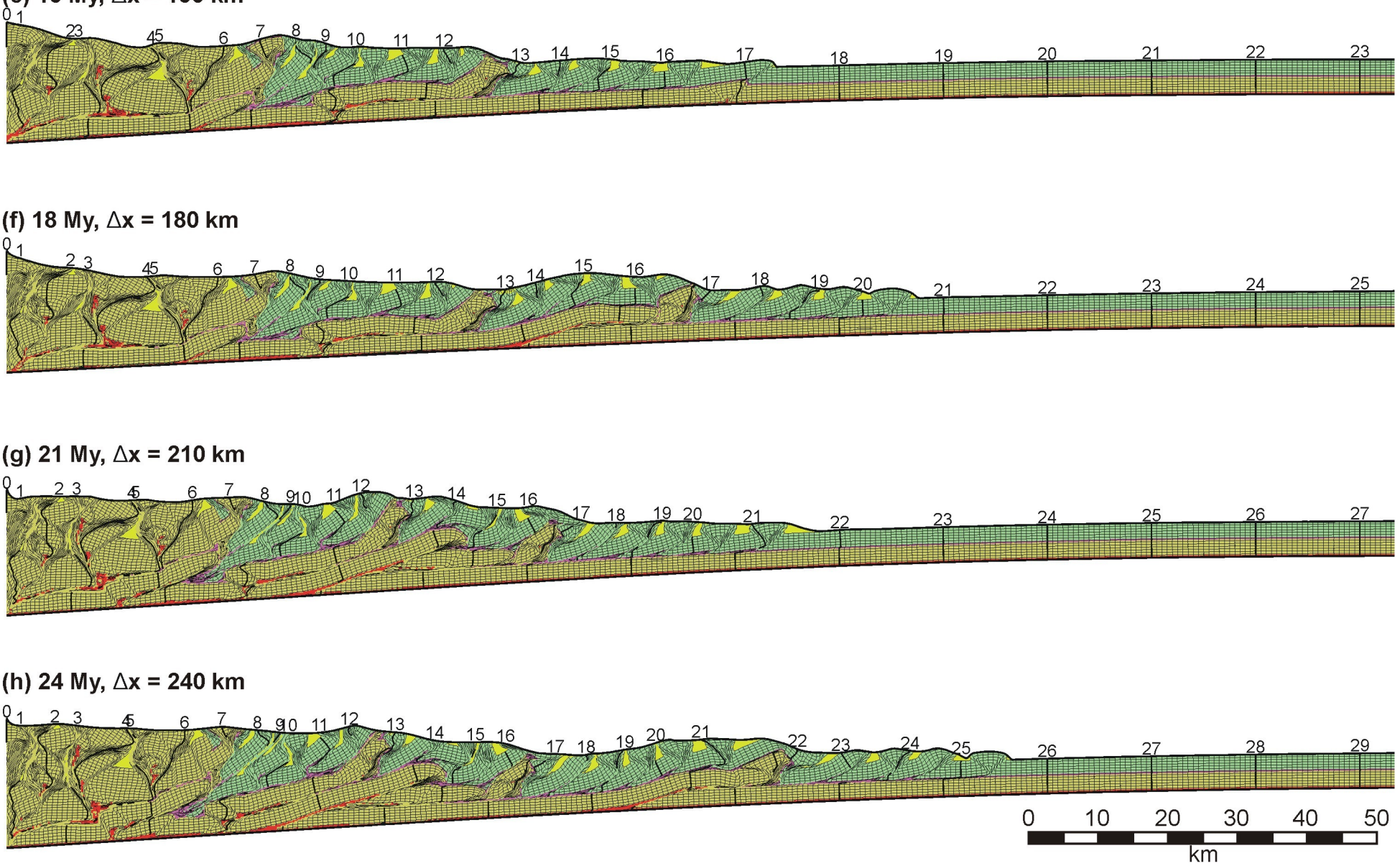

Stockmal et al., Figure 7, part 2 (Price vol).

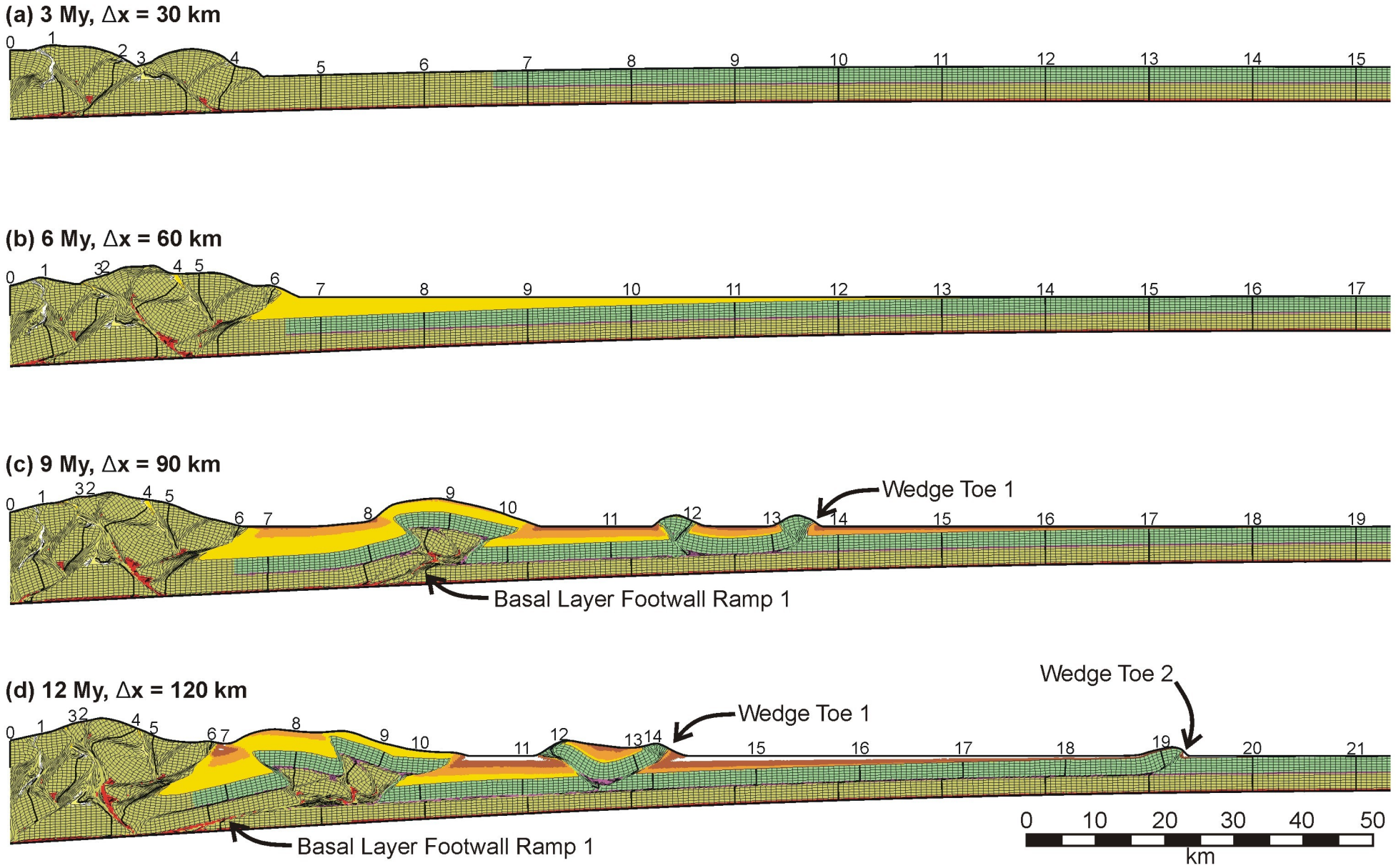

Stockmal et al., Figure 8, part 1 (Price vol).

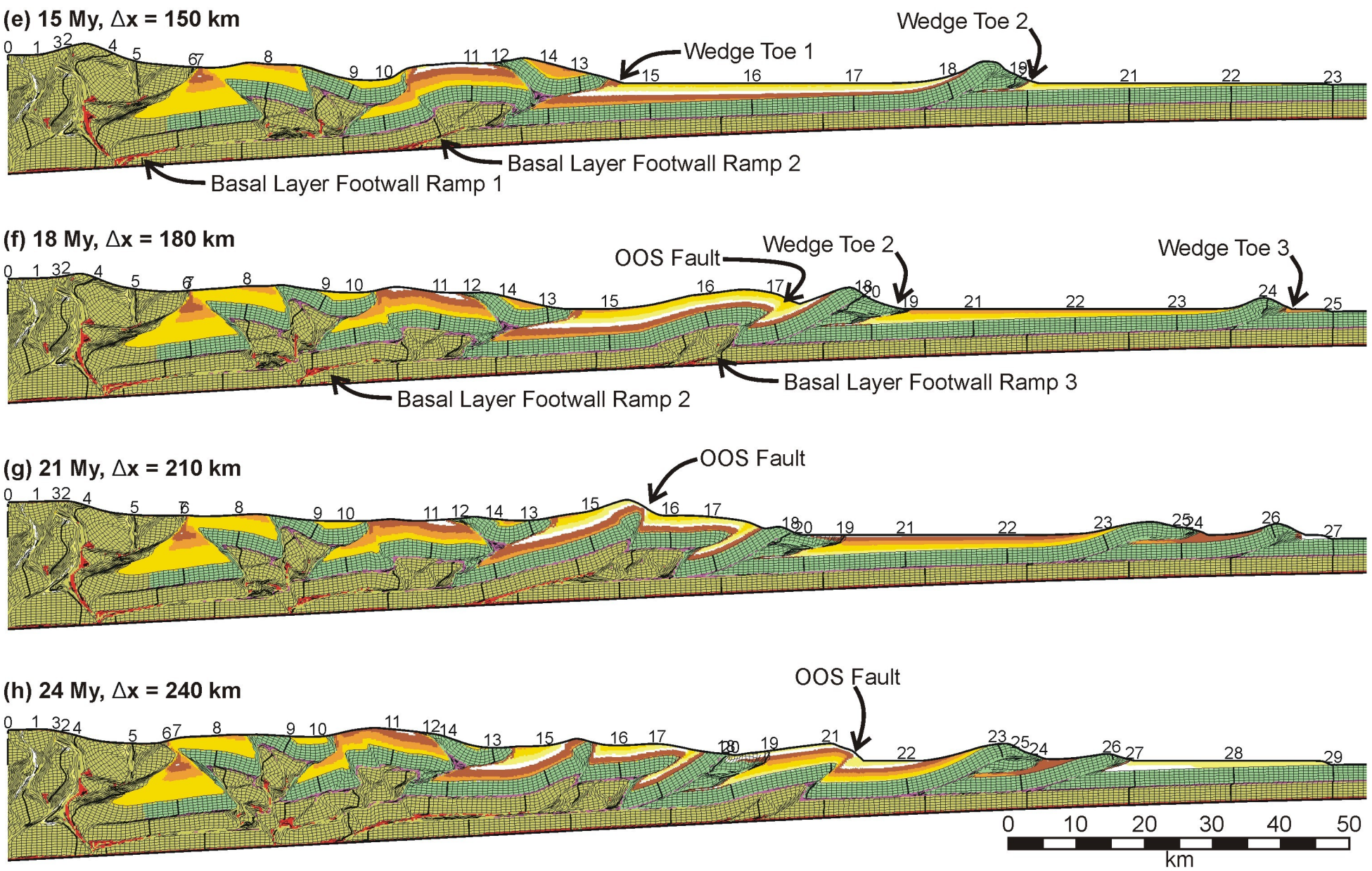

Stockmal et al., Figure 8, part 2 (Price vol).

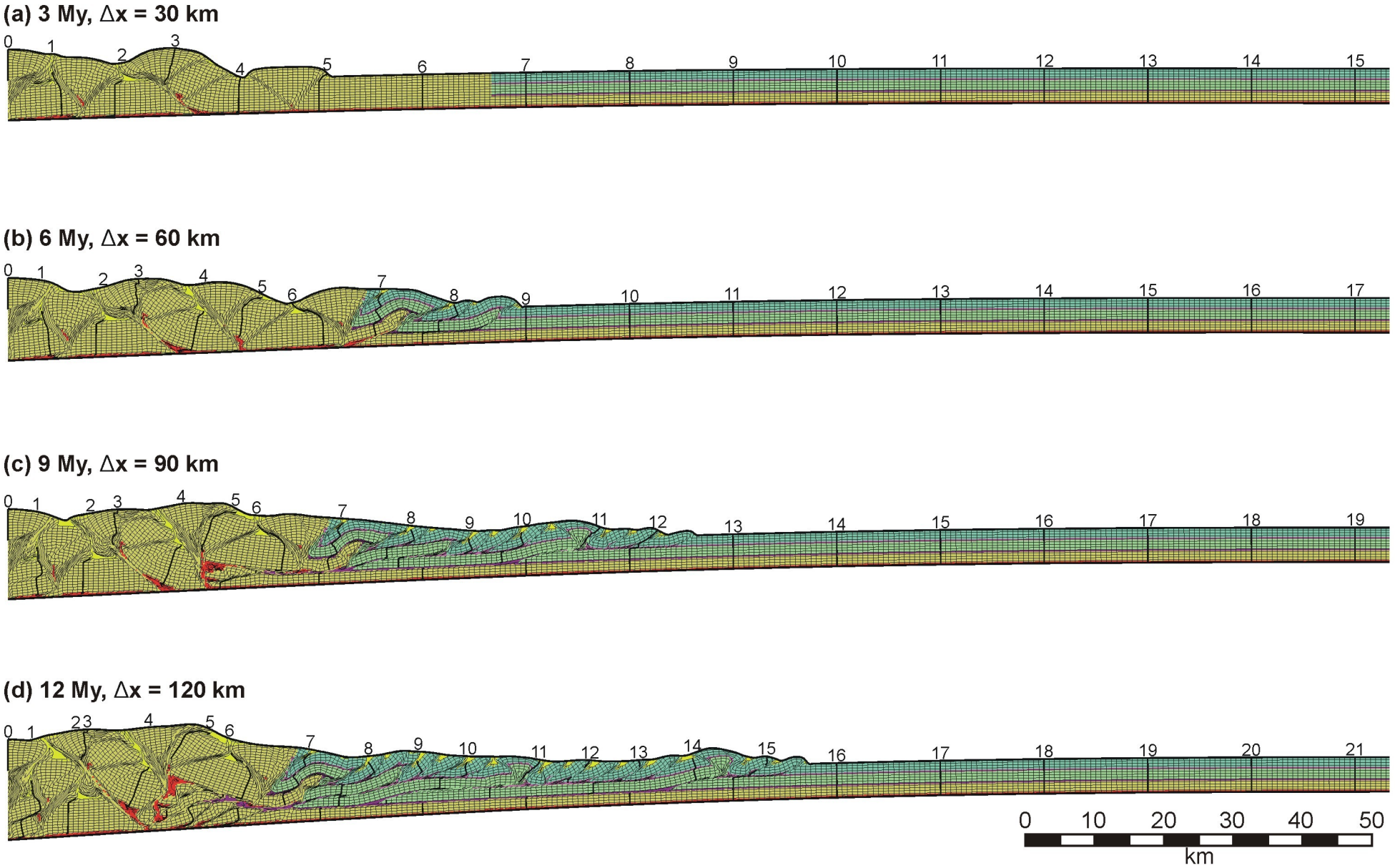

Stockmal et al., Figure 9, part 1 (Price vol).

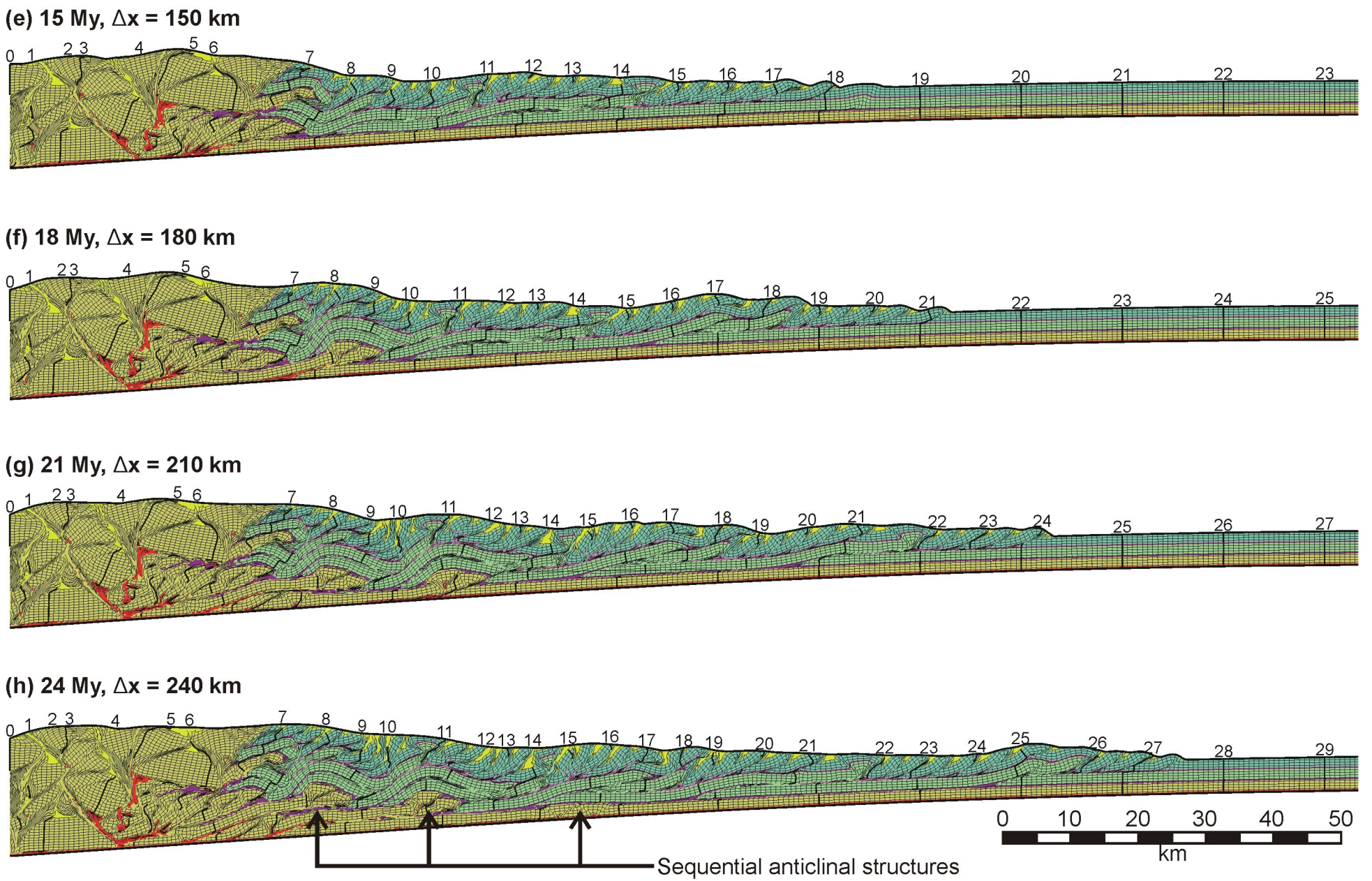

Stockmal et al., Figure 9, part 2 (Price vol).

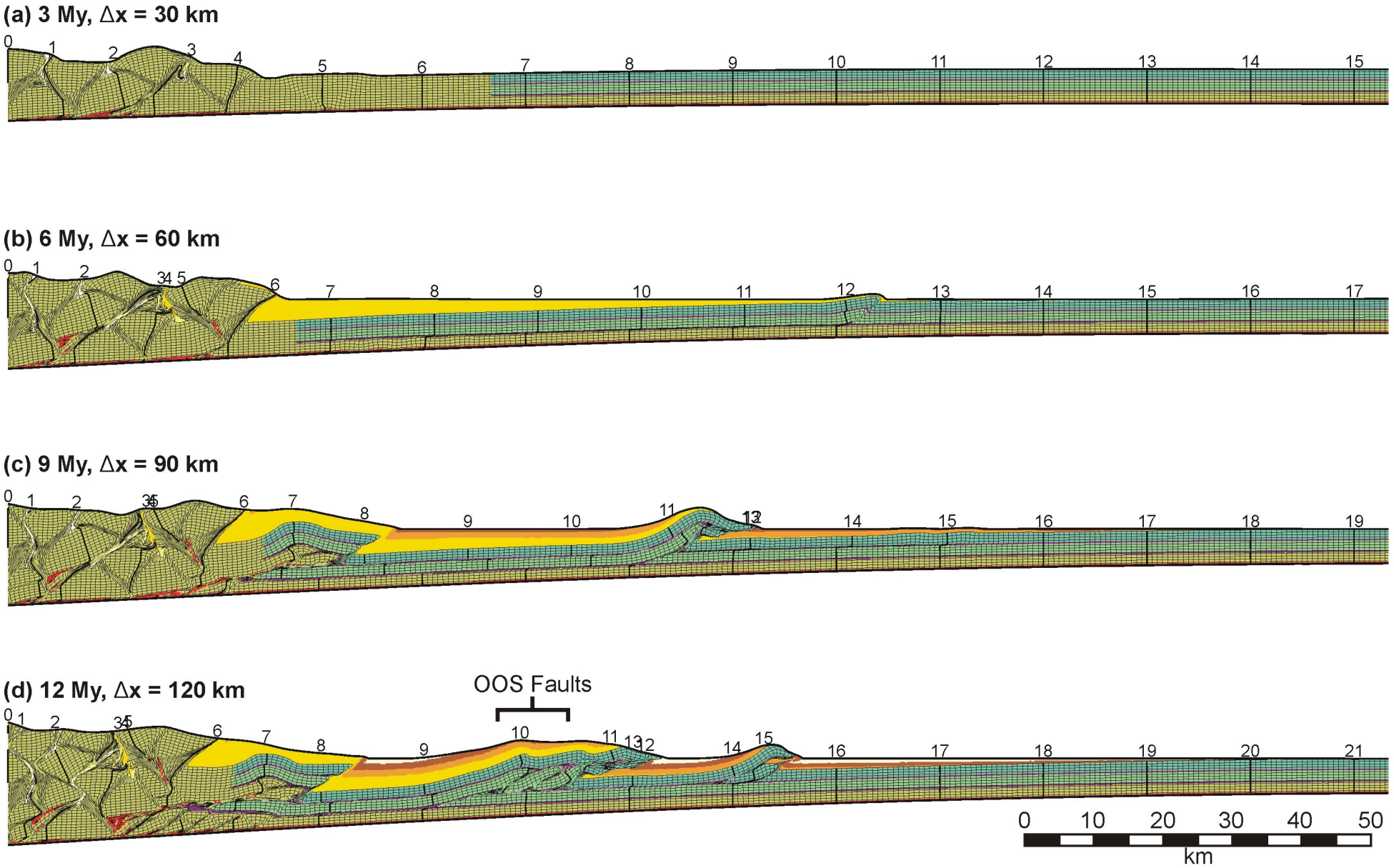

Stockmal et al., Figure 10, part 1 (Price vol).

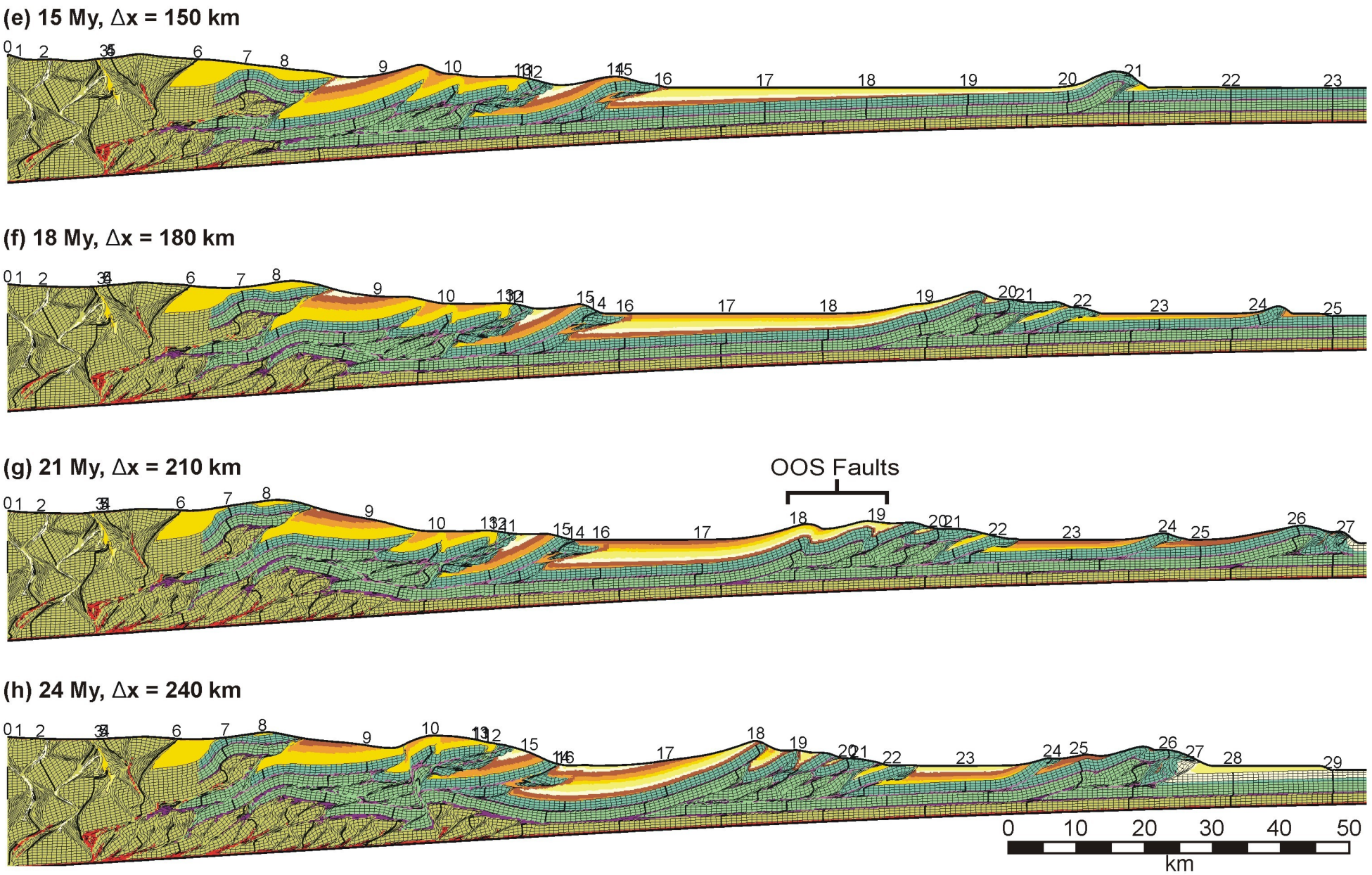

Stockmal et al., Figure 10, part 2 (Price vol).

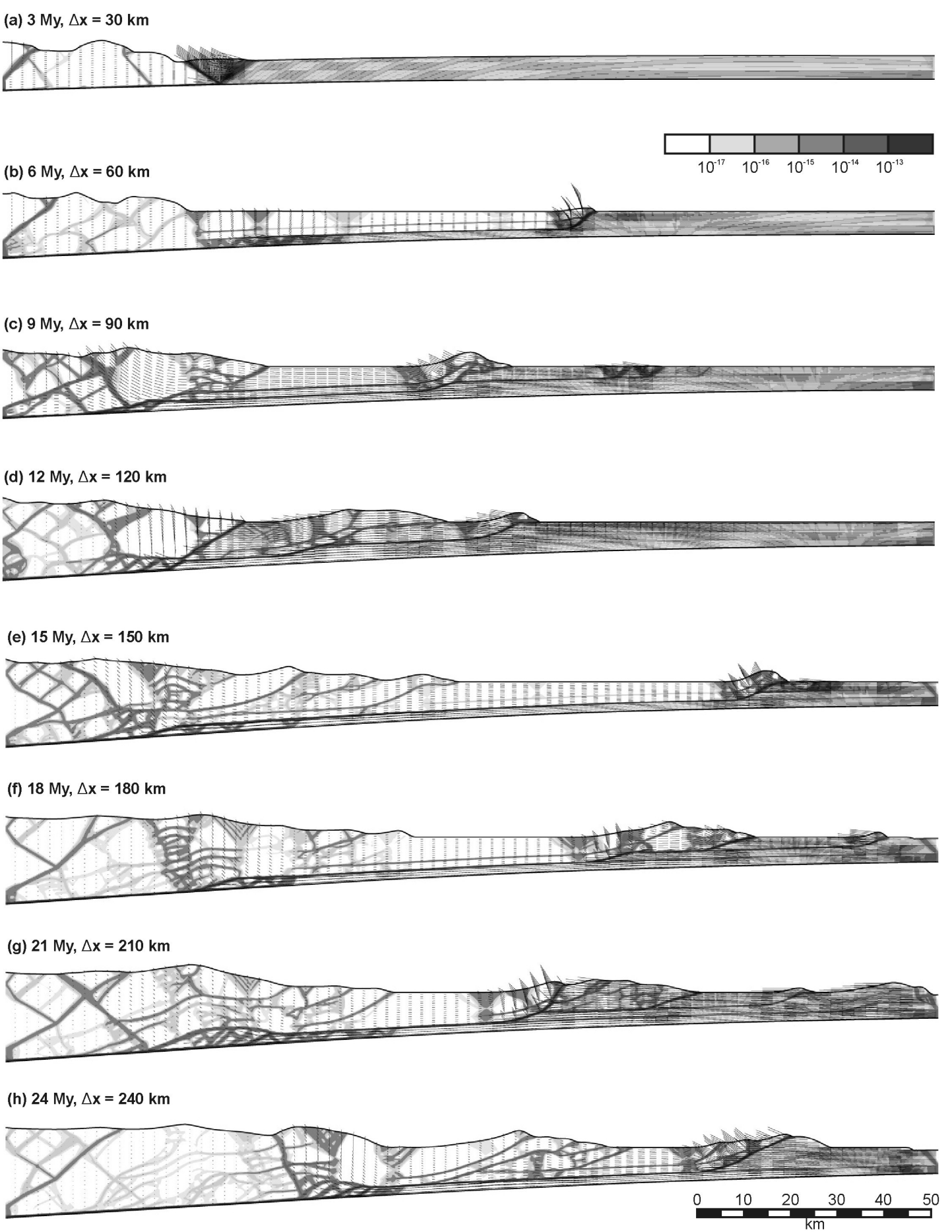

Stockmal et al., Figure 11 (Price vol).

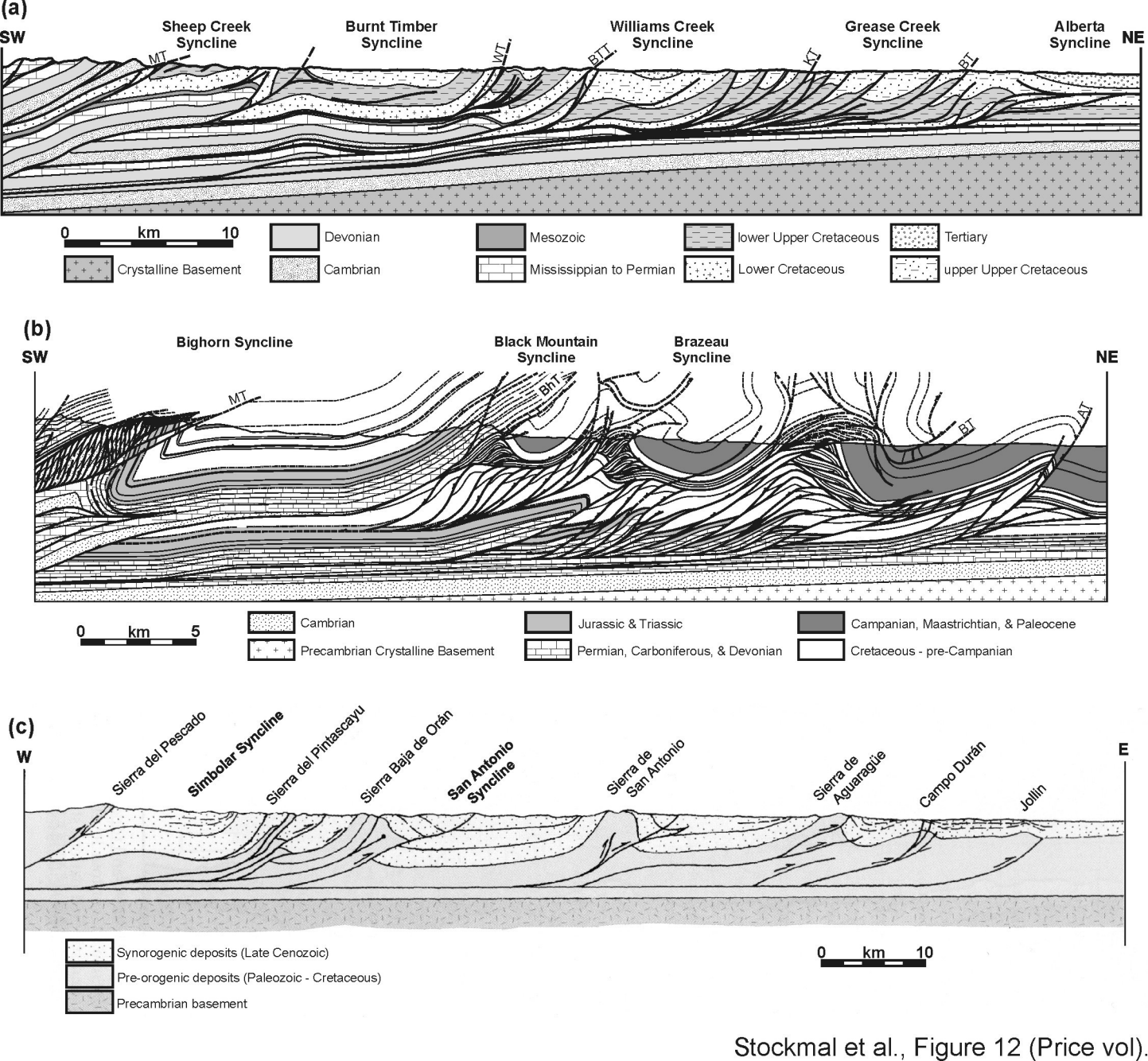

Stockmal et al., Figure 12 (Price vol).

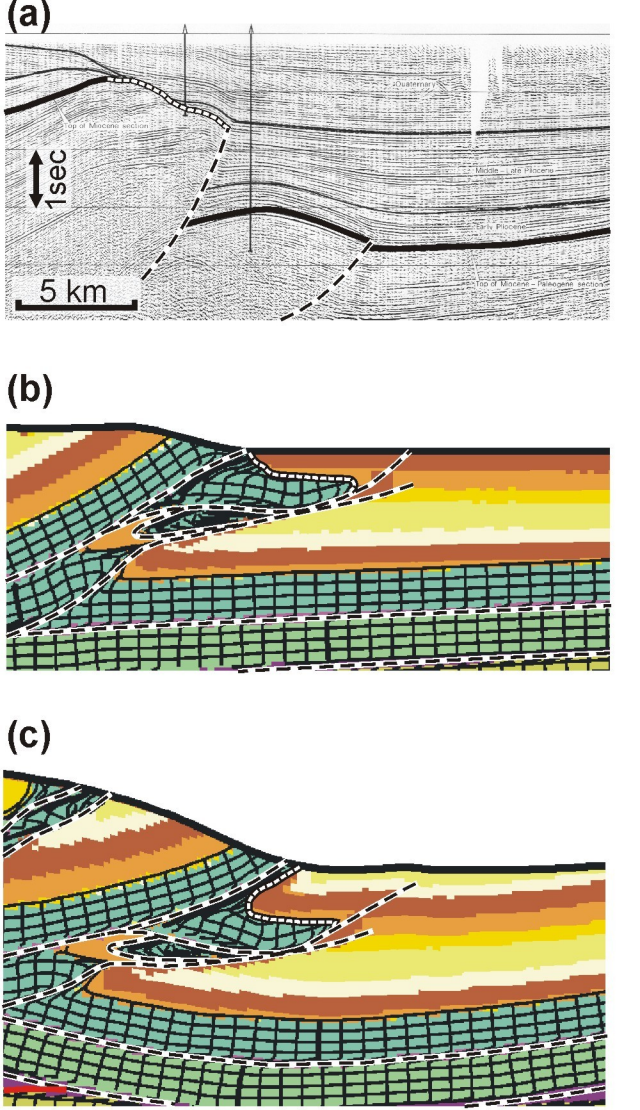

Stockmal et al., Figure 13 (Price vol).

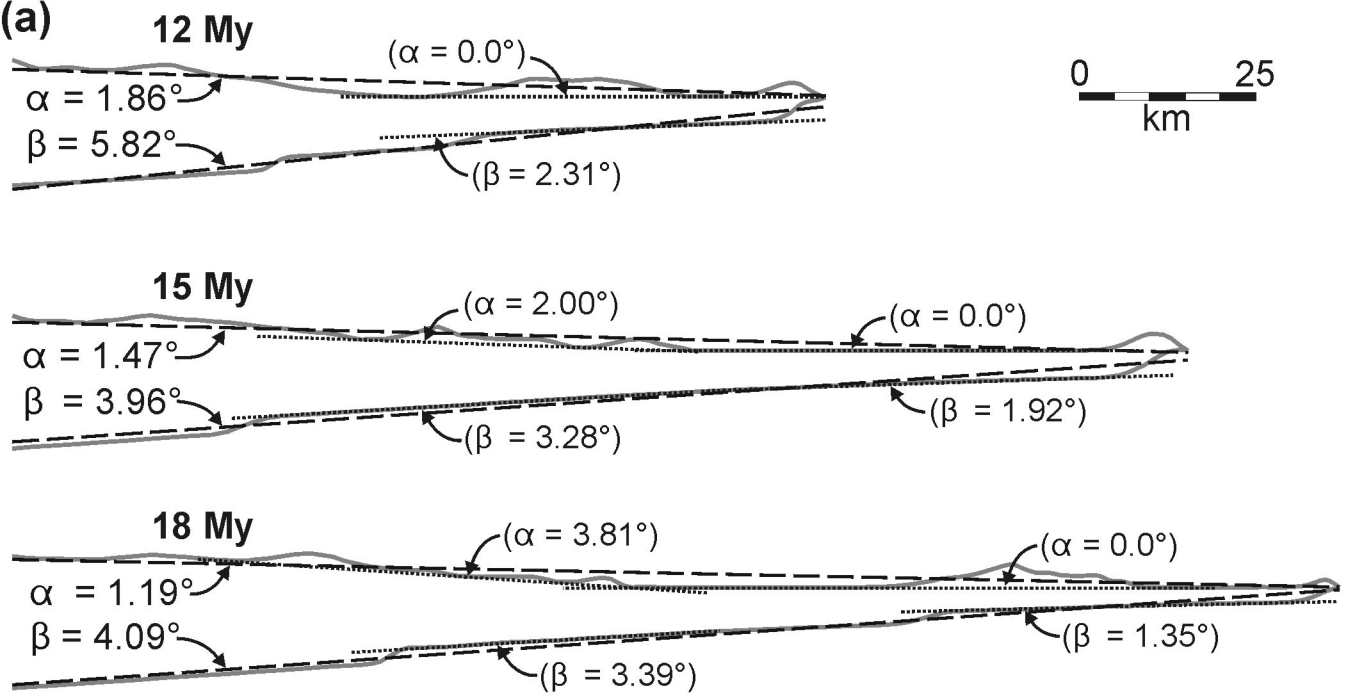

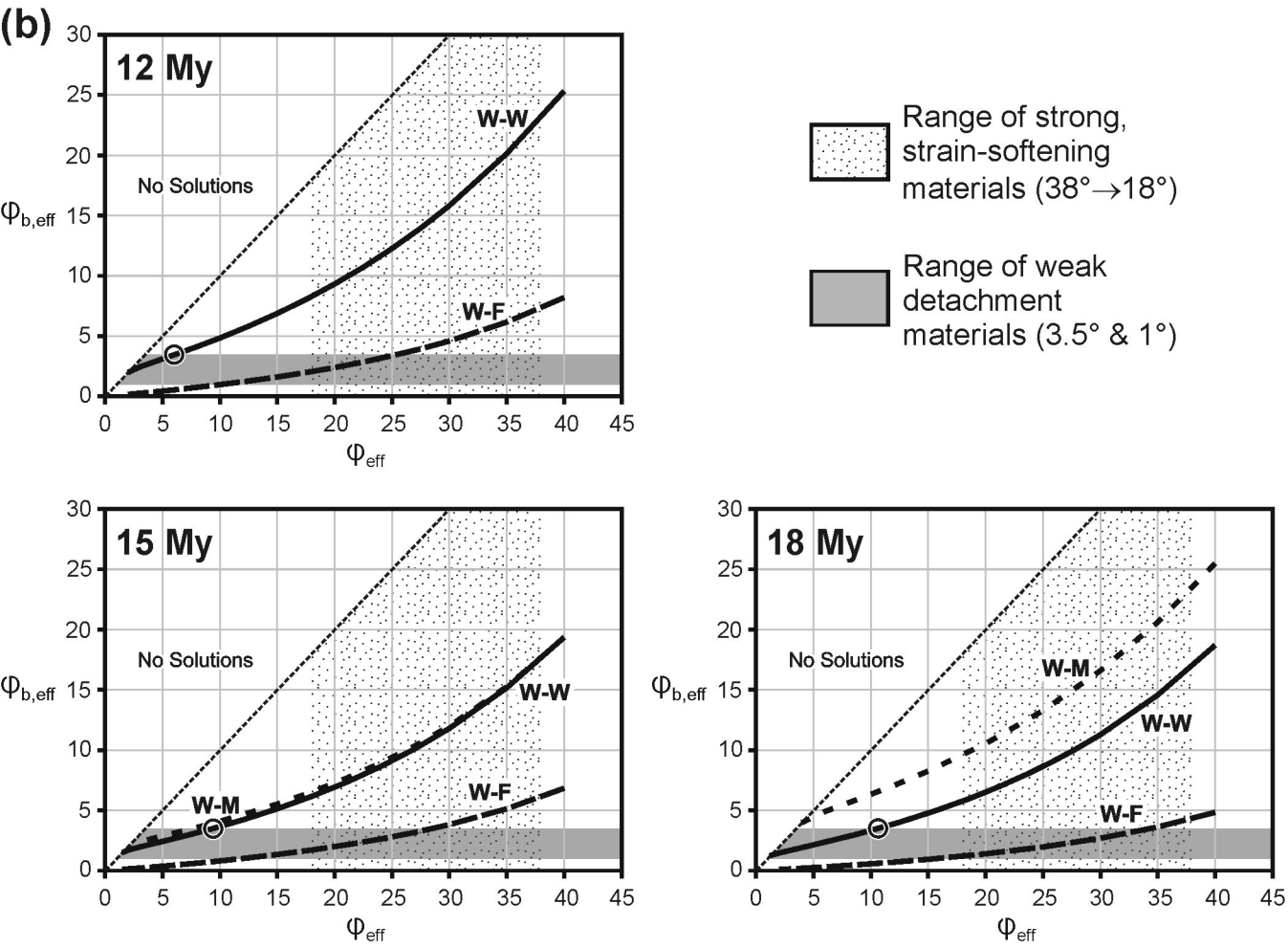

Stockmal et al., Figure 14 (Price vol).